

4

TECHNICAL REPORT BRL-TR-3003

**BRL**

DENSE HEAVY METAL AEROSOL MONITORING  
BY DIRECT X-RAY FLUORESCENCE

GEORGE M. THOMSON

JUNE 1989

**SDTICD**  
ELECTE  
JUN 16 1989  
CH

APPROVED FOR PUBLIC RELEASE; DISTRIBUTION UNLIMITED.

U.S. ARMY LABORATORY COMMAND

BALLISTIC RESEARCH LABORATORY  
ABERDEEN PROVING GROUND, MARYLAND

AD-A209 077

89

0

13

279

DESTRUCTION NOTICE

Destroy this report when it is no longer needed. DO NOT return it to the originator.

Additional copies of this report may be obtained from the National Technical Information Service, U.S. Department of Commerce, Springfield, VA 22161.

The findings of this report are not to be construed as an official Department of the Army position, unless so designated by other authorized documents.

The use of trade names or manufacturers' names in this report does not constitute indorsement of any commercial product.

UNCLASSIFIED

SECURITY CLASSIFICATION OF THIS PAGE

## REPORT DOCUMENTATION PAGE

Form Approved  
OMB No. 0704-0188

1a. REPORT SECURITY CLASSIFICATION UNCLASSIFIED			1b. RESTRICTIVE MARKINGS		
2a. SECURITY CLASSIFICATION AUTHORITY			3. DISTRIBUTION / AVAILABILITY OF REPORT		
2b. DECLASSIFICATION / DOWNGRADING SCHEDULE			APPROVED FOR PUBLIC RELEASE; DISTRIBUTION UNLIMITED		
4. PERFORMING ORGANIZATION REPORT NUMBER(S) BRL-TR-3003			5. MONITORING ORGANIZATION REPORT NUMBER(S)		
6a. NAME OF PERFORMING ORGANIZATION Ballistic Research Laboratory		6b. OFFICE SYMBOL (If applicable) SLCBR-TB-EP		7a. NAME OF MONITORING ORGANIZATION	
6c. ADDRESS (City, State, and ZIP Code) Aberdeen Proving Ground, MD 21005-5066			7b. ADDRESS (City, State, and ZIP Code)		
8a. NAME OF FUNDING / SPONSORING ORGANIZATION Ballistic Research Laboratory		8b. OFFICE SYMBOL (If applicable)		9. PROCUREMENT INSTRUMENT IDENTIFICATION NUMBER	
8c. ADDRESS (City, State, and ZIP Code) Aberdeen Proving Ground, MD 21005-5066			10. SOURCE OF FUNDING NUMBERS		
			PROGRAM ELEMENT NO. / 62618A	PROJECT NO. AH80	WORK UNIT ACCESSION NO. 001AJ
11. TITLE (Include Security Classification) DENSE HEAVY METAL AEROSOL MONITORING BY DIRECT X-RAY FLUORESCENCE					
12. PERSONAL AUTHOR(S) George M. Thomson					
13a. TYPE OF REPORT TECHNICAL REPORT		13b. TIME COVERED FROM _____ TO _____		14. DATE OF REPORT (Year, Month, Day) JUNE 89	
15. PAGE COUNT 43					
16. SUPPLEMENTARY NOTATION					
17. COSATI CODES			18. SUBJECT TERMS (Continue on reverse if necessary and identify by block number)		
FIELD	GROUP	SUB-GROUP	Aerosol Monitoring, Dust Detector, X-ray Fluorescence		
19	01	01			
24	01				
19. ABSTRACT (Continue on reverse if necessary and identify by block number) Dense aerosols are widely found as active ingredients or byproducts in pyrotechnics, explosives, obscurants, antipersonnel munitions, and rocket engines. The Ballistic Research Laboratory (BRL) is applying a state-of-the-art microanalytical tool, x-ray fluorescence, to a new task of monitoring the mass concentrations of dense aerosols containing metals. The results obtained promise a solution for a long-standing problem in metal aerosol work - the necessity of extracting particles out of the air prior to assessment in a fashion that gives samples that are truly representative of the aerosol. The new method works directly on the dispersed aerosol and provides noninvasive concentration measurements rapidly, simply, and reliably for most materials with atomic number above 24. The potential of the direct x-ray fluorescence method has been evaluated in tests targeting a two-dimensional simulant iron aerosol. The results show that, in a minute or less, one can assess aerosol concentrations from a few milligrams up to several grams per cubic meter. Higher sensitivities can be readily realized if increased x-ray doses can be tolerated. Based on these findings, developing a more advanced instrument appears worthwhile.					
20. DISTRIBUTION / AVAILABILITY OF ABSTRACT <input checked="" type="checkbox"/> UNCLASSIFIED/UNLIMITED <input type="checkbox"/> SAME AS RPT. <input type="checkbox"/> DTIC USERS			21. ABSTRACT SECURITY CLASSIFICATION UNCLASSIFIED		
22a. NAME OF RESPONSIBLE INDIVIDUAL George M. Thomson			22b. TELEPHONE (Include Area Code) (301) 278-4905		22c. OFFICE SYMBOL SLCBR-TB-EP

DD Form 1473, JUN 86

Previous editions are obsolete.

SECURITY CLASSIFICATION OF THIS PAGE

UNCLASSIFIED

## ACKNOWLEDGEMENTS

The author gratefully acknowledges the contributions of Margret Kahl, a BRL cooperative education student, in many facets of this effort including preparing the targets, taking preliminary data, and preparing raw results for computer analysis. Similar appreciation is extended to another student, Susan Giglio-Tos, for her help in the detector response studies and in the data processing work.



Accession For	
NTIS GRA&I	<input checked="" type="checkbox"/>
DTIC TAB	<input type="checkbox"/>
Unannounced	<input type="checkbox"/>
Justification	
By	
Distribution/	
Availability Codes	
Dist	Avail and/or Special
A-1	

## ABSTRACT

Dense aerosols are widely found as active ingredients or byproducts in pyrotechnics, explosives, obscurants, antipersonnel munitions, and rocket engines. The Ballistic Research Laboratory (BRL) is applying a state-of-the-art microanalytical tool, x-ray fluorescence, to a new task of monitoring the mass concentrations of dense aerosols containing metals. The results obtained promise a solution for a long-standing problem in metal aerosol work -- the necessity of extracting particles out of the air prior to assessment in a fashion that gives samples that are truly representative of the aerosol. The new method works directly on the dispersed aerosol and provides noninvasive concentration measurements rapidly, simply, and reliably for most materials with atomic number above 24. The potential of the direct x-ray fluorescence method has been evaluated in tests targeting a two-dimensional simulant iron aerosol. The results show that, in a minute or less, one can assess aerosol concentrations from a few milligrams up to several grams per cubic meter. Higher sensitivities can be readily realized if increased x-ray doses can be tolerated. Based on these findings, developing a more advanced instrument appears worthwhile.

## CONTENTS

	<u>Page</u>
LIST OF FIGURES .....	vii
1 INTRODUCTION .....	1
2 GENERAL PRINCIPLES .....	2
3 THE APPARATUS .....	4
3.1 General features .....	4
3.2 The demountable x-ray tube .....	5
3.2.1 General considerations .....	5
3.2.2 Mechanical features .....	9
3.2.3 Electrical features .....	11
3.2.4 Vacuum features .....	13
3.3 The target .....	13
3.3.1 Design considerations .....	13
3.3.2 Target construction .....	18
3.4 The detectors .....	18
3.4.1 SiLi detectors .....	18
3.4.2 Proportional counters .....	20
3.5 The analysis system .....	22
4 THE EXPERIMENT .....	26
5 RESULTS .....	29
5.1 Iron targets .....	29
5.2 Copper targets .....	32
5.3 Tests at higher voltages .....	33
6 CONCLUSIONS AND SUGGESTIONS .....	33
7 REFERENCES .....	36
DISTRIBUTION LIST .....	37

## LIST OF FIGURES

<u>Figure</u>	<u>Page</u>
1. A direct x-ray fluorescence aerosol monitor . . . . .	3
2. Copper x-ray tube output spectra at 14 kV, 25 kV, and 35 kV . . . . .	7
3. The spectral effect of a 0.0025-cm-thick Zr film acting on the output of a germanium tube . . . . .	8
4. Photographs of the x-ray tube exterior (upper), cover (center), and interior (lower) . . . . .	10
5. The electrical layout of the x-ray tube . . . . .	12
6. The layout of aerosol simulant target and the x-ray tube . . . . .	14
7. The x-ray tube illumination geometry . . . . .	15
8. The calculated simulant distance for Fe and Cu targets plotted versus the distance from the tube at which the x-rays enter the detector's field of view . . . . .	19
9. The x-ray spectra output by a SiLi detector when Fe-loaded (upper) and blank (lower) targets are fluoresced with germanium x-rays . . . . .	21
10. The x-ray spectra output by a proportional counter when Fe-loaded (upper) and blank (lower) targets are fluoresced with gold x-rays . . . . .	23
11. The x-ray spectra output by a SiLi detector when Fe-loaded (upper) and blank (lower) targets are fluoresced with gold x-rays . . . . .	24
12. A block diagram of the detection-analysis electronics. The output-pulse shape is depicted above each active component . . . . .	25
13. An improved direct fluorescence device . . . . .	35

## 1. INTRODUCTION

Soldiers have always had to contend with dust- and smoke- laden air. Even though history records many instances in which aerosols have been used as tactical obscurants, it was not until this century and the advent of modern technology that the full potential of metal aerosols as combat tools was realized. Aerosolized, finely-divided metals and their compounds are now a key ingredient in fuel-air explosives, pyrotechnics, reaction engines, chemical munitions and obscurants. Central to all applications of metal aerosols is a measurement of their metal's mass concentration. This report introduces a new concept for treating this problem.

Before proceeding, a definition of the term "dense, heavy-metal aerosol" is in order. For present purposes, it is an aerosol in which the suspended particles must meet three necessary criteria:

- a. be so finely divided that they remain airborne for a significant period of time.
- b. contain metals (or other heavy elements), preferably with atomic number  $Z > 24$ , either in pure, alloyed, or compounded form.
- c. be concentrated in the aerosol to the degree that a readily, measurable change in some bulk property of the aerosol as a whole takes place. Such properties may include transparency, chemical activity, density, dielectric strength, etc. For present purposes a concentration of at least  $1 \text{ mg/m}^3$  is implied.

Presently many aerosol-concentration measurement techniques exist. Most are based on a process called sampling<sup>1</sup> in which particles extracted from the air are deposited on a collection media. The simplest samplers are gravimetric, that is, devices allowing the particles to settle out of the aerosol by their own weight onto a collection surface, such as adhesive paper. More often, collection speed and efficiency is enhanced by forcing the aerosol through a filter paper at a given rate. Once the aerosol has been sampled, an appropriate means must be selected for determining how much material was taken out of the known volume of air. These techniques range in complexity from simply weighing the material, to more complex mass-sensitive methods using vibrating crystals,<sup>2</sup> to photometric measurements of filter blackening,<sup>3</sup> to absorption of beta



particles,<sup>4</sup> and even to atomic absorption or emission spectroscopy.<sup>5</sup> A few techniques exist that work directly upon the aerosol as dispersed and do not require sampling. Among the most well-known of these are ionization<sup>6</sup> and laser beam scattering-transmission.<sup>7</sup>

All the methods cited above suffer drawbacks. Any sampling-based technique must be accomplished in a way that the accumulated sample on the filter is representative of the aerosol. Errors can be introduced by flow inhomogeneities, captures in the sampler plumbing, filter penetrations, or particle escape. On the other hand, in direct methods, the quantity used to establish the presence of particles often is not simply and directly related to concentration. As examples of the latter case, consider either laser beam scattering or absorption; both are functions of the physical properties of the particles and the nature of the probing beam. Clearly, appropriate corrections, which are often complex, must be applied here and are usually required of any assay.

In this report we describe and evaluate a new method for noninvasive measurement of aerosol concentration called direct x-ray fluorescence (DXRF). Assessment of the DXRF concept involved construction of a proof-of-principle apparatus and its use in a series of preliminary experiments. The results indicate that DXRF can give rapid, accurate, and reliable concentration measurements in circumstances when the scrutinized aerosol has a component with  $Z > 24$  at a concentration greater than a few milligrams per cubic meter. Perhaps the most important of DXRF's advantages is that it virtually eliminates the need for collection media, pumps, and plumbing associated with sampling apparatus. It is also independent of particle size, shape, and even its state of detailed chemical combination. The following pages detail DXRF's principles, the proof-of-principle apparatus, the feasibility measurements and their results. The report concludes with a short discussion of some of the implications and limitations for a working tool based upon this principle, and finally, with an outline of additional work needed to exploit it.

## 2. GENERAL PRINCIPLES

The overall layout of a DXRF device is illustrated in Figure 1. The apparatus consists of three assemblies, an x-ray tube, a detector, and an analyzer. Simply put, the device uses x-rays from a very low power x-ray tube to irradiate the aerosol, photoionizing the inner shells of the metal atoms it contains. The resulting ions with inner shell vacancies are unstable. They

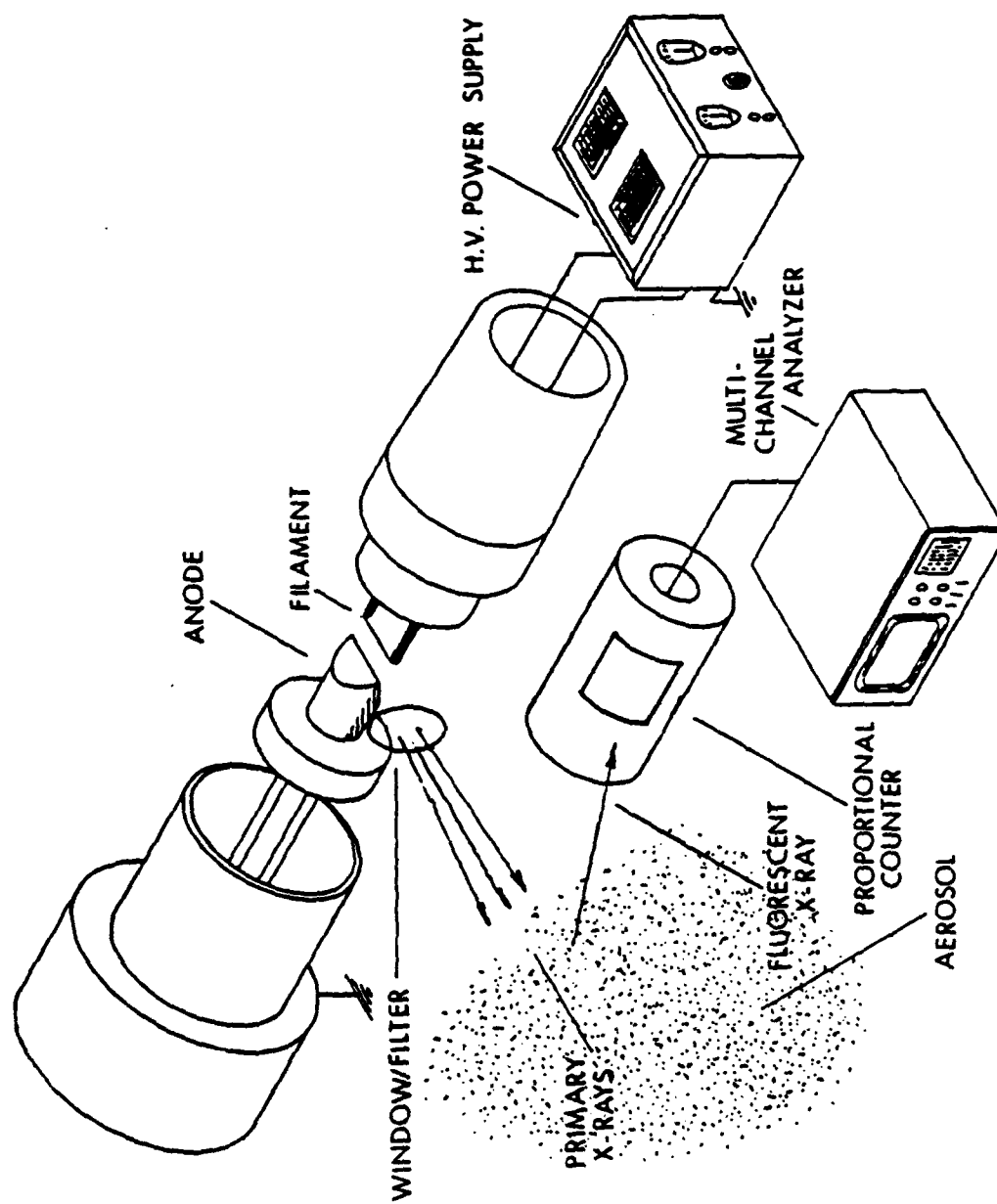


Figure 1. A direct x-ray fluorescence aerosol monitor.

spontaneously fill their vacancies through an immediate rearrangement of the remaining electrons. Often the rearrangement results in the emission of an x-ray photon at an energy that is characteristic of the emitting species. The overall photoionization-radiation process is called x-ray fluorescence. If x-rays coming from such an excited aerosol are spectrally analyzed by plotting the counts recorded as a function of x-ray energy, distinct peaks appear. The location and height of these peaks may be used in a totally straightforward procedure to determine the identities of the heavier elemental species present and their individual abundances, respectively. The underlying method, that is, x-ray fluorescence (XRF), is a common laboratory microanalytical tool. Only recently has it found use in real-time aerosol work,<sup>8</sup> and then only in relatively complex devices geared for concentrations in the microgram per cubic meter regime, which employ pumps and sampling methods. The innovation described in this report is that XRF can work directly on a dispersed aerosol, bypassing sampling.

Our task is then threefold:

- a. To assess the overall response of a direct x-ray fluorescence (DXRF) apparatus to some aerosols which may demonstrate its military potential.
- b. To determine the lower limit of concentration measurable with DXRF for such cases.
- c. To devise guidelines for selecting optimal combinations of x-ray tube and detector parameters for a given aerosol.

### 3. APPARATUS

3.1 Overall considerations. To carry out an empirical evaluation of the direct fluorescence concept, we have recently constructed a proof-of-principle device similar to that illustrated in Figure 1. The preliminary nature of this study precluded full-scale testing of the apparatus in a large test chamber. Instead, a two-dimensional target was designed that would induce the same response in our detection apparatus as would three-dimensional aerosols with known properties. The design and features of each of the major apparatus assemblies and of the simulated aerosol are discussed in the following few sections.

### 3.2 The demountable x-ray tube.

3.2.1 Design factors. The demountable x-ray tube is a low-power radiographic device specifically designed to allow selection of the intensity and energies of its x-ray photon output. With this ability maximum aerosol fluorescence and minimum extraneous scattered signals may be obtained, while assuring that the exciting (primary) and fluorescent photons are separated sufficiently in energy to allow unambiguous identification.

As with most x-ray tubes, the present device is essentially a high-voltage thermionic diode consisting of an electron emitting filament (cathode) and a grounded metal anode. When operating, the filament is maintained at a high negative potential with respect to ground. Consequently, any electrons leaving the filament are accelerated toward the anode through an evacuated gap and strike the anode's surface at an energy (in electronVolts) that is virtually identical to the accelerating potential. If an electron's acquired energy is greater than the binding energy of the anode atom's inner shell electrons, then its impact sometimes collisionally ionizes the shell. Like their photonionization-induced counterparts discussed earlier, these vacancies may also be filled through the emission of x-ray photons. Their individual photon energies equal that of the difference between the binding energies of an electron in the vacant inner shell and that of one in a higher shell. These values are, of course, a function both of the elemental identity of the anode and of the particular shells involved.

Figure 2 shows the spectral output of the present x-ray tube equipped with a copper anode and operated at accelerating potentials  $V$  of 14 kV, 25 kV and 35 kV. Each of the curves in Figure 2 is arbitrarily normalized to a fixed number of counts under the two, sharp characteristic x-ray lines of copper at 8.0 and 8.9 keV. These lines result from the filling of a 1s vacancies by electrons from the 2p ( $K\alpha$ ) and 3p ( $K\beta$ ) subshells, respectively. Unfortunately the passage of an electron into the anode material also results in a second type of radiation, bremsstrahlung, which arises from the accelerations the fast electrons suffer when they pass close to the anode material nuclei. The radiation appears over a range of energies extending almost up to that of the incident electron. It is well-known that both the broad bremsstrahlung peak and the characteristic peaks grow as the accelerating voltage  $V$  is raised. Note from Figure 2, however, that the latter does so at a faster

rate. Also, note that the most energetic portion of the bremsstrahlung peak becomes increasingly prominent as  $V$  increases. It is found empirically<sup>9</sup> that the characteristic radiation intensity grows with  $V$  according to the relation

$$I_c \propto (V-E_k)^{1.63} e^{-0.095Z} i \quad (1)$$

where  $E_k$  is the binding energy of a K shell electron;  $Z$  is the anode atomic number, and  $i$  is the anode current. The continuous bremsstrahlung energy spectrum, on the other hand, follows a relation giving the number of x-ray photons per unit energy interval  $dI_b/dE$ :

$$\frac{dI_b}{dE} \propto \frac{Z (V-E) i}{E} \quad (2)$$

where  $E$  is the photon energy.<sup>10</sup>

The limit on DXRF's ability to detect small mass concentrations arises because a small fraction of the bremsstrahlung radiation backscatters from the air into the detection apparatus. Some of the scattered component has the same energy as the sought-after fluorescent photons and may mask their presence. Masking may be at least partially alleviated by adjusting the relative contributions of bremsstrahlung and characteristic x-rays to the overall spectrum; that is, one must achieve maximum characteristic production under the constraint of minimum bremsstrahlung output at the fluorescent x-rays energy. This may be carried out in two ways -- by changing the operating voltage or by inserting an absorption filter over the x-ray tube's output aperture. In the first case, a rise in tube voltage brings with it an increased likelihood of electrical breakdown both inside and outside the tube, requiring an upscaling in the size and design complexity of components. Filters, on the other hand, achieve spectral purity by paying for it with a reduction in x-ray flux. The trick here is to gain the best suppression of bremsstrahlung at the fluorescent energy with the smallest loss of tube characteristic x-rays. An illustration of filter performance is given in Figure 3, which shows two energy spectra of x-rays backscattered by air irradiated by our x-ray tube. For these runs the tube had a germanium anode. The solid curve corresponds to no filter over the tube output. The dashed curve, on the other hand, was acquired using a 0.0025-cm-Zr-foil output filter.

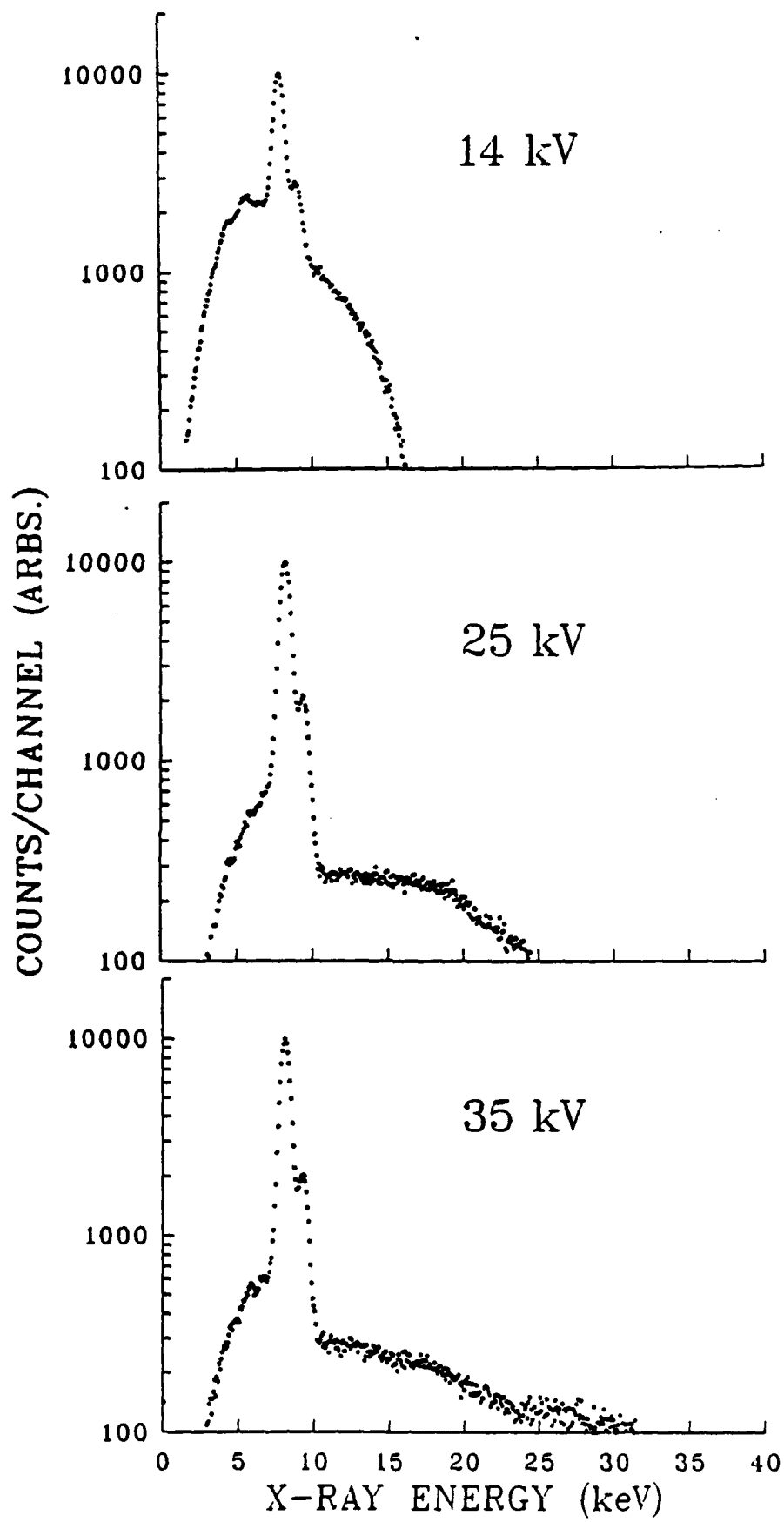


Figure 2. Copper x-ray tube output spectra at 14 kV, 25 kV & 35 kV.

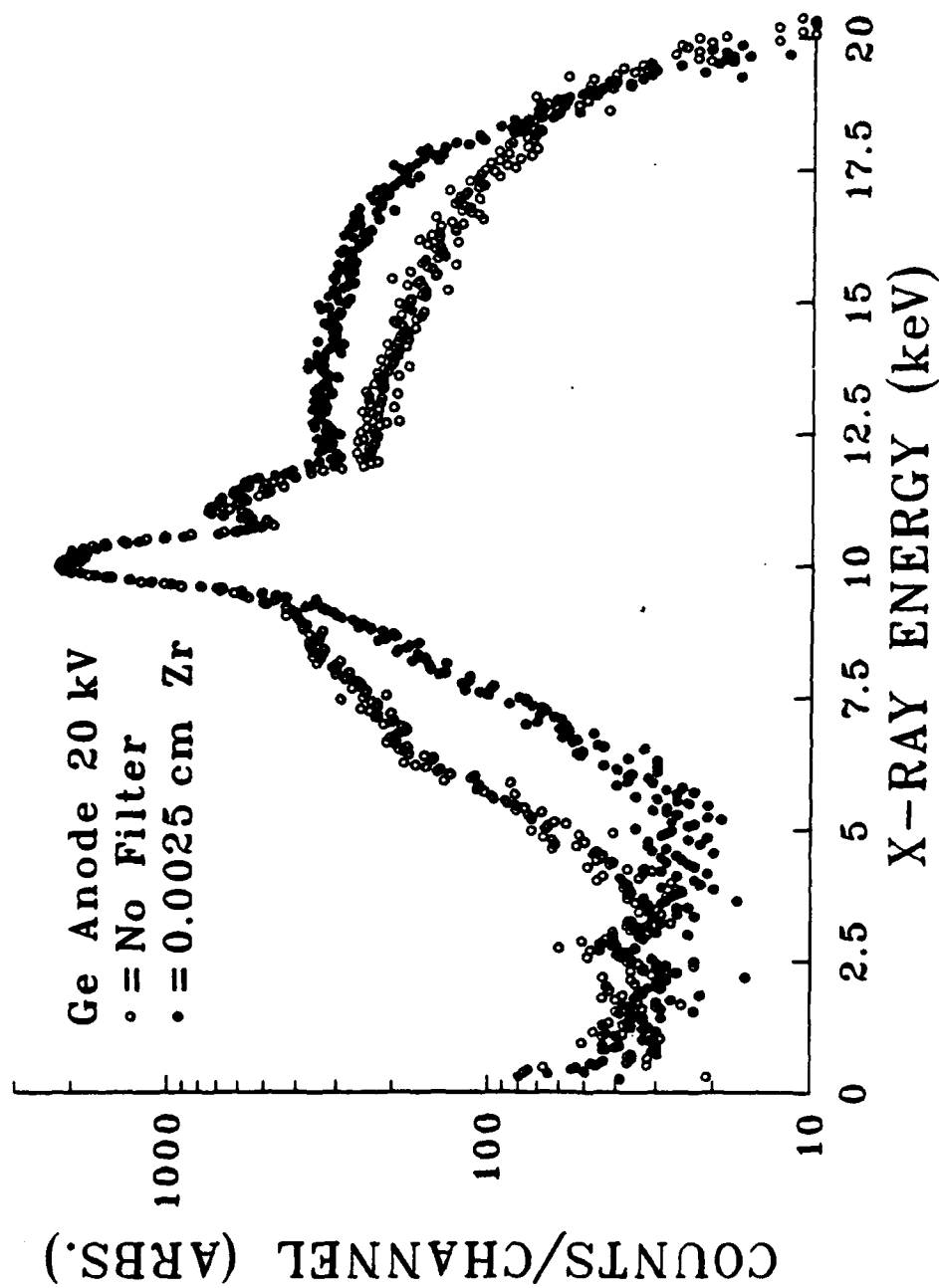


Figure 3. The spectral effect of a 0.0025-cm-thick-Zr film acting on the output of a germanium tube.

The heights of the characteristic Ge-K lines are again arbitrarily set equal so that the regions near iron K can be compared. Note that, at that location (near 6 keV), the relative background has been reduced by roughly a factor of three.

It also should be mentioned here that, at least theoretically, it is possible for characteristic x-rays to scatter from air inelastically and perhaps achieve energy losses and direction changes of the right magnitude to produce a masking signal. To guard against this possibility we examined the air-backscattered energy spectra of x-rays produced by two kinds of radioactive sources --  $\text{Fe}^{55}$  and  $\text{Cd}^{109}$ . Both derive their x-rays via K capture and presumably are bremsstrahlung-free. Our spectra indicate that neither produce any significant inelastic backscatter contribution except at energies immediately below those of their characteristic lines (5.9, 6.4 and 22.1, 24.9 keV, respectively). It is reasonable to infer that in the present experiment all inelastic, scattered characteristic x-ray effects are insignificant because the range of interest is bracketed by the  $\text{Fe}^{55}$  and  $\text{Cd}^{109}$  x-rays.

**3.2.2 Mechanical features.** Turning now to the mechanical aspects of the x-ray tube itself, refer to Figure 4, a photograph showing both its exterior and interior features. The tube's external structure consists of four components, the cathode cap-feedthru, the anode cap, the glass insulating column, and the external plastic support sleeve. The cap assemblies are thick, cylindrical aluminum structures supporting their respective elements and providing coupling to external electrical and cooling services. The anode cap also incorporates connections to external high vacuum pumps and ports through which the x-ray flux exits. Each cap is maintained at the potential of the corresponding element. They are separated both electrically and mechanically by a thick coaxial glass tube that also combines with the caps to form a high-vacuum container. Surrounding the entire outside of the combination is another coaxial cylinder made of lucite. This sleeve provides a safe level of electrical insulation around all high-voltage elements and supports the entire assembly.

The interior active elements of the x-ray tube are its heated filament (cathode) and the anode. Their relative locations are best seen in Figure 1. Considering the filament first, it is composed of a 0.025-cm-diameter tungsten wire mounted between and perpendicular to the rounded ends of two



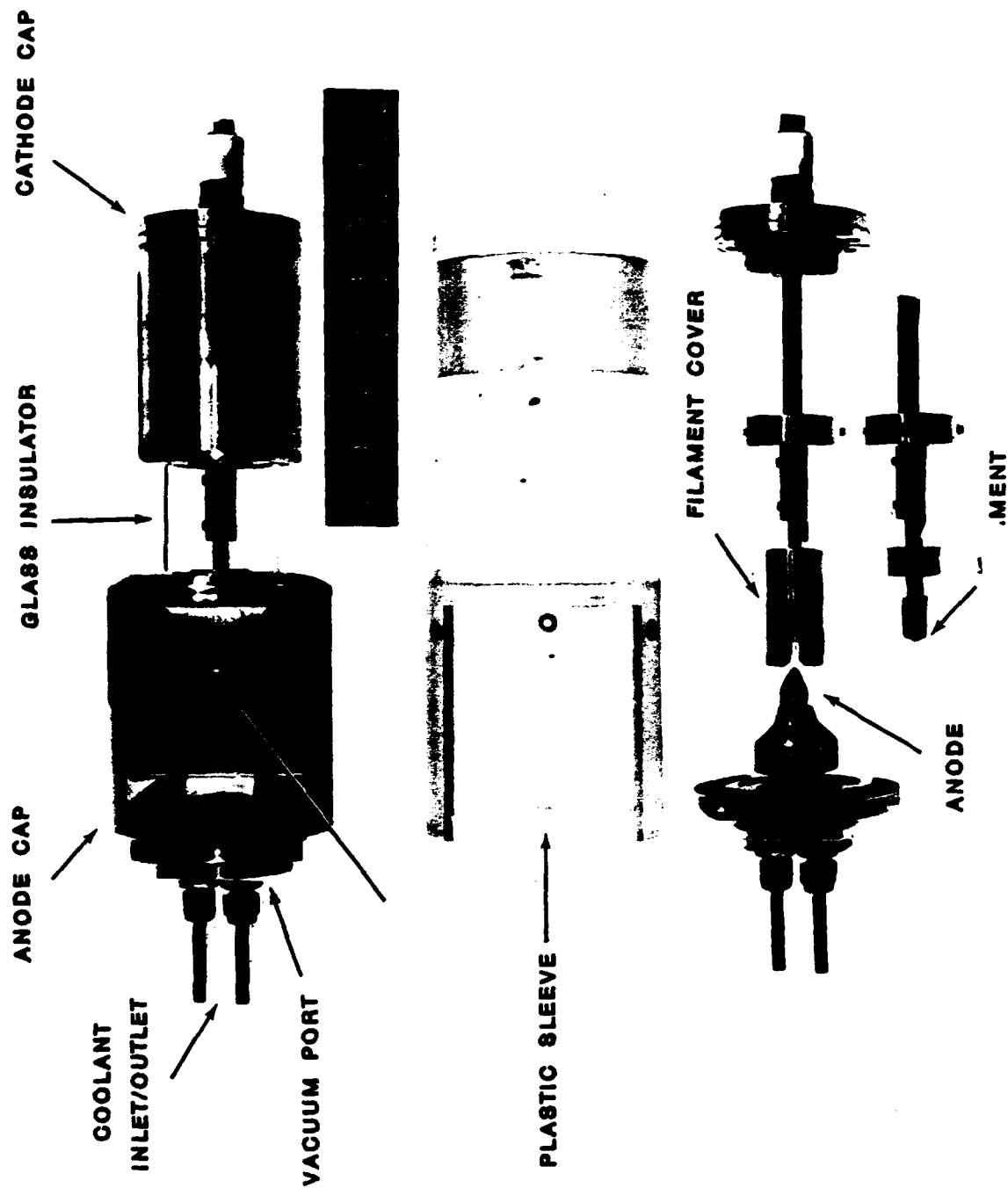


Figure 4. Photographs of the x-ray tube exterior (upper), cover (center), and interior (lower).

parallel rods. The filament axis lies parallel to the front edge of a thin, small, wedge-shaped slice of material comprising the anode. Approximately 0.3 cm separate these two elements. The dual-line, filament-anode arrangement makes our tube inherently self-focusing, reducing the x-ray source size over more conventional planar arrays. The inherently self-focusing tube does, however, deposit a relatively large amount of energy into a small volume of anode. To minimize the resultant heating, the anode is firmly held between the jaws of a small, cylindrical aluminum clamp, which, is mounted at the center of a hollow copper, water-cooled jacket. This configuration permits, not only the easy interchange of various anodes of different materials without any extensive fabrication, but also the use of anode materials having a relatively low melting point. Another design advantage was gleaned by inclining the axis of the filament and the leading edge of the anode at an angle of approximately 6 degrees to the line perpendicular to the tube axis. When viewed from the side, as one would from the output window, the electron-impacted section of the anode does not appear as a line, but as an intensely radiative dot. The small apparent source size makes it easy to calculate the illumination geometry using point-source approximations, eliminating such troublesome effects as penumbral shadows. Finally, the tube is arranged so that x-rays emitted along the proper azimuth from the focal spot exit the evacuated region through a 0.0025-cm-thick aluminum window into the surrounding air. A smaller aperture directly opposite the window allows one to extract a small x-ray flux for purposes of monitoring tube-output levels.

3.2.3 Electrical features. The electrical layout of the tube is illustrated in Figure 5. The operating high voltage comes from a power supply which can deliver up to 50 mA at 50 kV. Simultaneously, the filament current is provided by a servo-driven, 10-VAC autotransformer connected across the output of a 1:1, 120-VAC isolation transformer. Use of this scheme allows one to float both leads of the filament at any desired negative high voltage and independently control the tube emission current. Feedback and regulation of the tube voltage and current are done manually. Both are monitored -- the first with a high voltage divider placed between the filament and ground, and the second with a millimeter interposed in the anode-ground path. For the present tasks the tube power levels are always less than a few tens of watts -- a power level that is far less than that of, say, a medical x-ray machine and the intrinsic capabilities of our power supplies. Nonetheless, the fact that this unit is run essentially continuously requires that due care be taken to prevent personnel exposure.

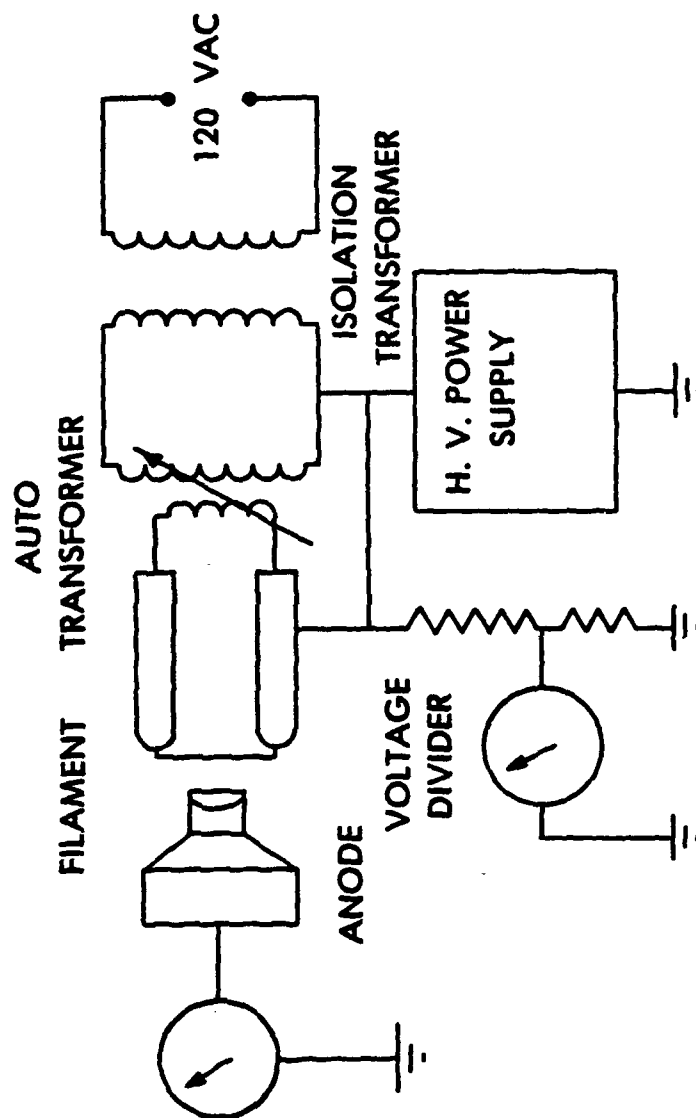


Figure 5. The electrical layout of the x-ray tube.

3.2.4 Vacuum features. The demountable anode feature of this x-ray tube mandates that it be provided with continuous vacuum service. A 5-cm oil diffusion pump-trap-forepump combination mounted on the anode cap provides this capability. Under normal operating conditions the pressure in the tube was approximately  $1 \times 10^{-6}$  mm Hg. The vacuum across the narrow filament-anode gap is critical in preventing electrical breakdown. In cases where the anode material is both a poor thermal conductor and has a low melting point (such as Germanium), breakdown can be induced when the surface of the electron-bombarded anode vaporizes and contaminates the gap. For refractories with good thermal conductivities, much higher power levels far in excess of present needs are possible.

### 3.3 The target.

3.3.1 Design considerations. As already mentioned, it was not possible in the limited scope of this work to conduct a full-scale evaluation of this apparatus in a large chamber. Instead, it was decided to construct a two-dimensional simulation of a dispersed aerosol that would produce an equivalent response in our detector. Our two-dimensional target consists of a stiff paper sheet at whose center is a circular region uniformly impregnated with a known amount of powdered metal. In use, the sheet is suspended with its plane perpendicular to the direction of the x-ray flux emanating from the tube at a given distance from its aperture (Figure 6). The circle is then illuminated with x-rays, and the intensity of the fluorescence output from its surface is monitored with a detector located at a point adjacent to the x-ray tube. It is the essential task of this section to find the distance  $x_0$  between the x-ray tube and the paper. We impose a further constraint. Specifically,  $x_0$  is the distance at which fluorescent counts from the target are equal to that one would derive from an aerosol whose mass concentration of the element sought in grams per cubic meter is numerically equal to the mass of metal in the circle on the paper.

Consider a conical volume of included angle  $\theta$  illuminated by a diverging flux of  $I_0$  photons per second entering from the x-ray tube. The x-ray detector is located very close to the source point and has an opening of area  $A$ . The situation is illustrated in Figure 7. At a distance  $x$  from the source, the x-ray flux drops to:

$$I = I_0 e^{-(\mu_c / \rho_a) \rho_a x} \quad (3)$$

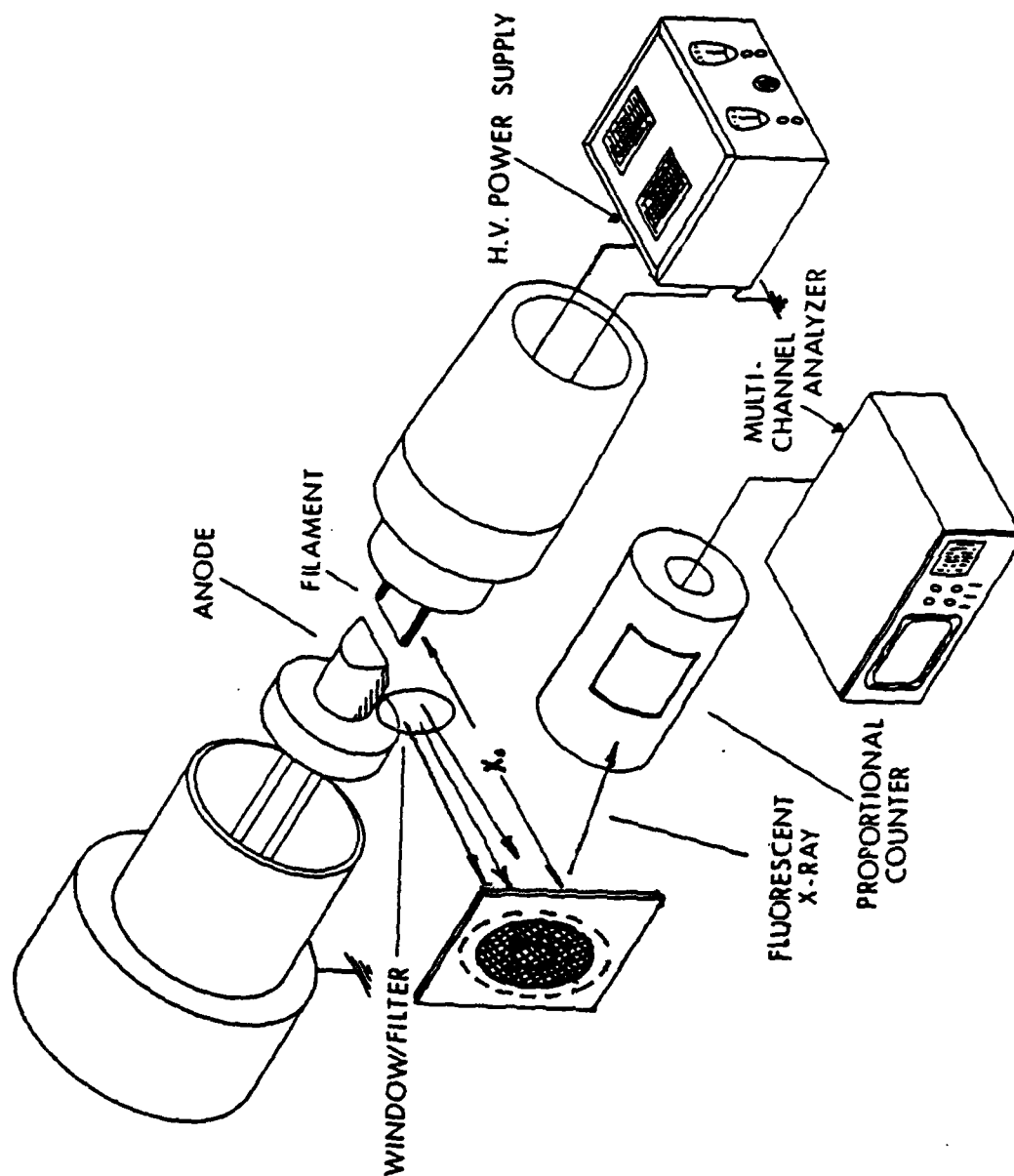


Figure 6. The layout of aerosol-simulant target and the x-ray tube.

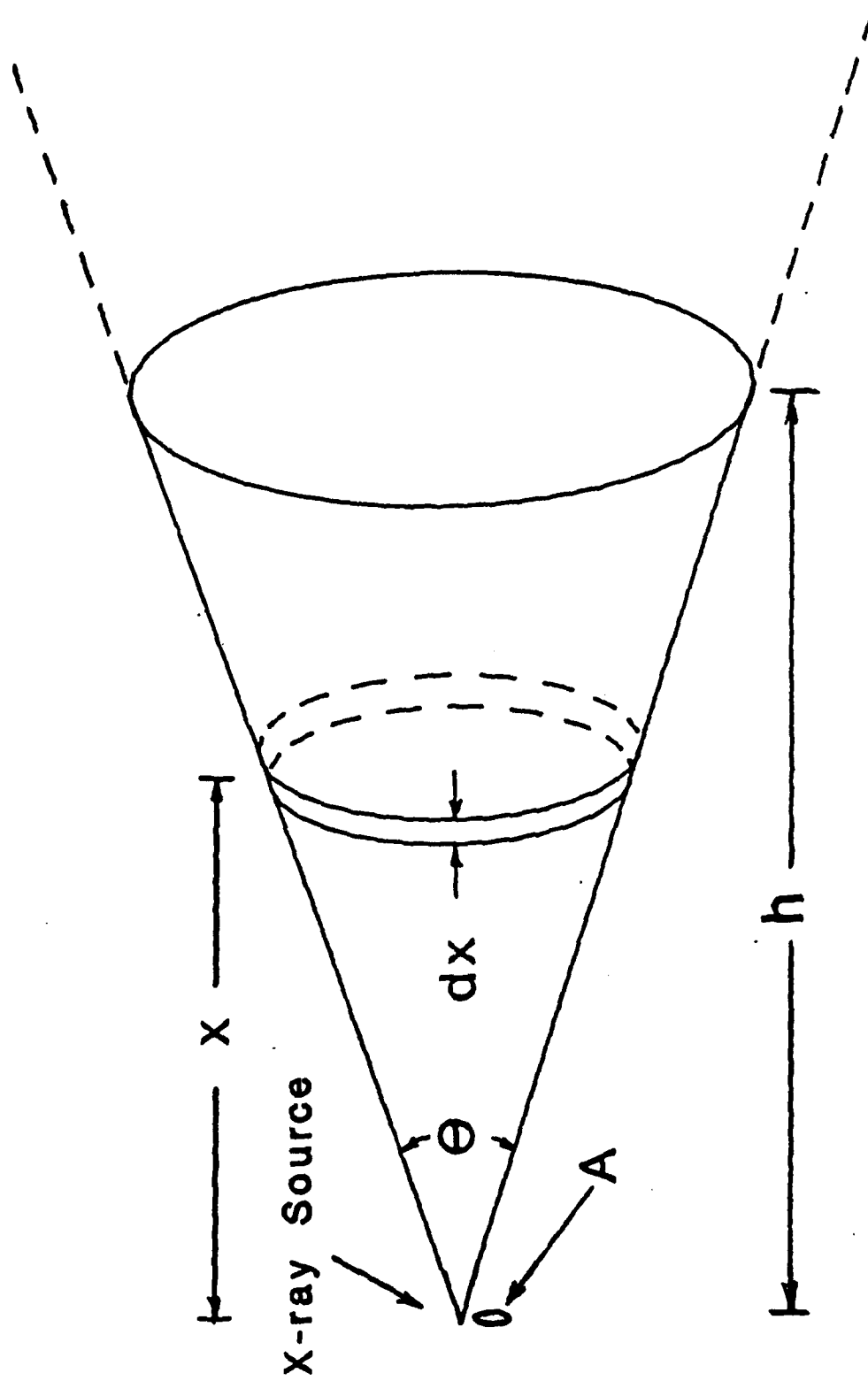


Figure 7. The x-ray tube illumination geometry.

where  $(\mu_c / \rho_a)$  is the mass attenuation coefficient for tube characteristic x-rays traveling in air and  $\rho_a$  is the density of air. In this exposition the assumption is made that attenuation is one-dimensional; that is, the  $\cos \theta = 1$  and axial paths are equal in length to paths on the cone's surface. The complete analysis shows that the error introduced by this assumption is a few percent as long as  $\theta$  is less than 30 degrees. While traversing the slice of the cone between  $x$  and  $x + dx$ , metal particles in the aerosol photoelectrically absorb a fraction  $(\tau_s / \rho_s) \rho_s dx$  of the remaining flux where  $(\tau_s / \rho_s)$  is the photoionization mass absorption coefficient for tube-characteristic x-rays traveling in the metal, and  $\rho_s$  is the density of the metal in the aerosol. Since we are concerned only with fluorescence, absorption processes other than photoionization -- the only process which creates significant numbers of inner shell vacancies -- are not important. The photoelectric loss of x-ray photons in the slab is approximately equal to the number of atoms in that volume with vacancies. Of that number, a fraction  $\omega$ , called the fluorescence yield, produce fluorescent x-rays. In other words,

$$I_0 e^{-(\mu_c / \rho_a) \rho_a x} (\tau_s / \rho_s) \rho_s \omega dx \quad (4)$$

fluorescent x-rays are created. To be counted these x-rays must now complete a return trip to the detector. Fluorescence emission is essentially isotropic. Thus, a fraction  $A/4\pi x^2$  head in the correct direction to gain entrance. However, of that number, only a fraction given by  $e^{-(\mu_f / \rho_a) \rho_a x}$  survive absorption by the air where  $(\mu_f / \rho_a)$  is the mass attenuation coefficient of x-rays with the energy of the fluorescent x-rays in air. The total fluorescent flux from all the slabs,  $C$ , can, of course, be evaluated by integration over  $x$  or:

$$I_f = \int I_0 e^{-\left(\frac{\mu_c}{\rho_a} + \frac{\mu_f}{\rho_a}\right) \rho_a x} \frac{A}{4\pi x^2} \left(\frac{\tau_s}{\rho_s}\right) \rho_s \omega dx \quad (5)$$

Before continuing let us consider the fluorescent x-ray flux detected if one substitutes a thin circle of metal at a distance  $x_0$  for the dispersed aerosol. This situation is shown in Figure 6. Assuming for the moment that the target disk has a small thickness, then the fluorescence,  $I_d$ , at area  $A$  from the disc is similar to the integrand above or:

$$I_d = I_o e^{-\left(\frac{\mu_c}{\rho_a} + \frac{\mu_f}{\rho_a}\right) \rho_s x_o - \frac{A}{4\pi x_o^2} \left(\frac{\tau_s}{\rho_s}\right) \bar{\rho}_s \omega \Delta x} \quad (6)$$

where  $\bar{\rho}_s$  is the density of the metal powder in the disc. We have, however, required that the amount of material on the disc be numerically equal to that in a cubic meter of aerosol; that is:

$$\bar{\rho}_s \pi x_o^2 \tan^2 (\theta/2) \Delta x = \rho_s \bar{V} \quad (7)$$

where  $\bar{V}$  has a numerical value of  $1 \text{ m}^3$ .  $\bar{V}$  is also the volume of a cone of included angle  $\theta$  and length  $h$  or  $\bar{V} = 1/3 \pi \tan^2 (\theta/2) h^3$ . Using Equation 7 and canceling factors of  $\pi \tan^2 \theta/2$ , we get

$$\bar{\rho}_s = \frac{\rho_s h^3}{3 x_o^2 \Delta x} \quad (8)$$

Letting  $D = \frac{I_o}{4\pi} A \left(\frac{\tau_s}{\rho_s}\right) \rho_s \omega$ , and  $G = -\left(\frac{\mu_c}{\rho_a} + \frac{\mu_f}{\rho_a}\right) \rho_s$ , we get

$$I_d = \frac{D h^3 e^{G x_o}}{3 x_o^4} \quad (9)$$

and the integral in Equation 6 becomes:

$$I_f = D \int \frac{e^{Gx}}{x^2} dx \quad (10)$$

which may be integrated by parts. That result may further be evaluated numerically or integrated analytically and it yields a series solution of the form:

$$-\frac{D}{x} e^{Gx} + DG \left[ \log x + Gx + \frac{G^2 x^2}{2 \cdot 2!} + \frac{G^3 x^3}{3 \cdot 3!} + \dots \right] \quad (11)$$



To effect a reasonable simulation of an aerosol with a two-dimensional target, one must find values of  $x_0$  that make  $I_d$  equal to  $I_f$ . The limits of integration extend from the point where primary x-rays enter the detector's field of view out to a distance that is so large, further expansion would offer only a negligible contribution. Values of  $x_0$  have been evaluated with a computer for numerous cases representing various possible detector geometries. Some results are shown in Figure 8 for iron and copper targets illuminated with germanium-K x-rays. It is these values which were then incorporated into the design of the feasibility experiment.

3.3.2 Target construction. Two targets, one of iron and one of copper, were constructed for the feasibility test. The target material itself consists of 1g of finely-divided reagent grade metal. After being uniformly distributed over a circle of the proper diameter marked on a piece of prepared paper, the powder was repetitively ground with a glass pestle until it was locked in securely. A microscopic examination shows that the particles become trapped in the paper's fibers. The loaded paper was next secured to a stiff cardboard frame, allowing the central disc to be accurately positioned in front of the x-ray tube. The distances  $x_0$  employed ranged from 40-60 cm depending upon anode and target species. In all tests the diameter of the cone of illumination was purposely kept approximately 20 percent larger than the diameter of the target circle (27 cm) to allow for any misalignment of the beam and target axes. Realizing that iron represents a more difficult situation, it was decided to subject that case to the bulk of experimental scrutiny.

### 3.4. The detectors.

3.4.1 Lithium-drifted, silicon (SiLi) detectors. In the present investigation two different types of devices are employed to detect the fluorescent x-rays. The first is a liquid, nitrogen-cooled, lithium-drifted silicon (SiLi) detector, namely an Ortec Model SLP-04170. Basically, a SiLi is a large reverse-biased p-n junction. When the semiconductor stops an ionizing photon, it has electron-hole pairs created within it. The reverse bias forces the pairs to separate and flow through external circuitry producing a measurable pulse. The number of electron-hole pairs and the resulting pulse height are proportional to the energy of the ionizing x-ray. SiLi's have good energy resolution, a feature that is useful for studying spectral details of filter performance, x-ray multiplets, etc. However, they also have a comparatively small entrance aperture, A, making them

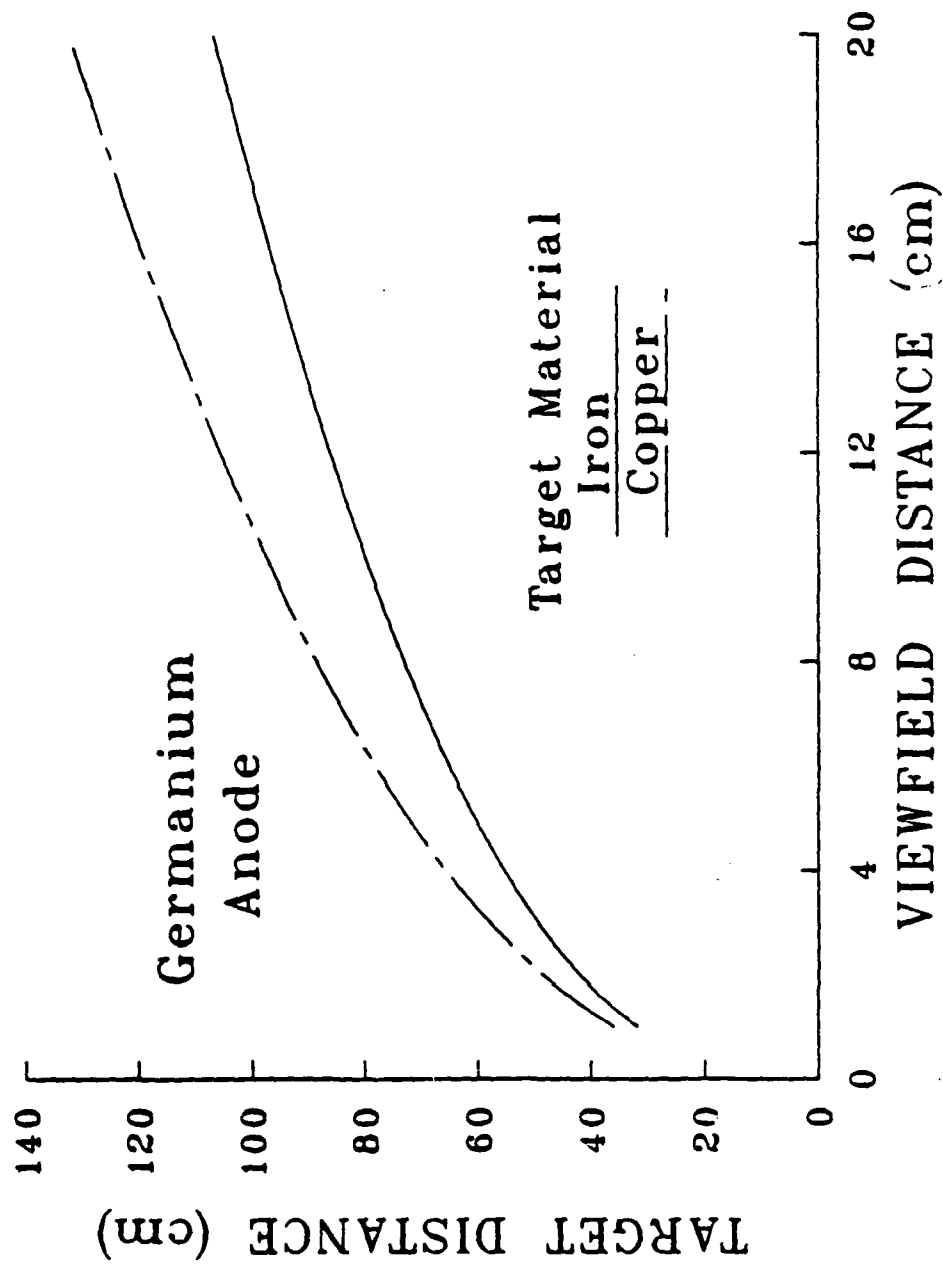


Figure 8. The calculated simulant distance for Fe and Cu targets plotted versus the distance from the tube at which the x-rays enter the detector's field of view.

very inefficient. This shortcoming is further compounded by the necessity of providing liquid nitrogen cooling to the detector. These factors pose design problems in any extensive field application. Other types of semiconductor detectors, such as intrinsic germanium, have been recently introduced that overcome some of these problems. Their present high cost, however, is prohibitive.

Figure 9 shows an example of the output of a SiLi detector looking at an iron target fluorescing under bombardment with Germanium-K x-rays. Note that it shows the K multiplets of iron -- lines separated by 0.65 keV (6.40 keV versus 7.05 keV) and the asymmetry of the primary Ge lines induced by some photon's "inelastic" scattering from air. Other examples of SiLi spectra have already appeared in Figure 2.

3.4.2 Proportional counters. A different device, which appears to have some features better suited to dense aerosol analysis, is the thin-wire gas proportional counter. In most configurations it consists of a gas-filled cylindrical tube equipped with a thin wire mounted along its axis. If a potential of 2-3 kV is established between the wall and the wire, then each time the gas is ionized by an incident x-ray photon, a cascading discharge occurs. Over a limited range of voltages the cascade multiplication is directly proportional to the energy of the incident x-ray and deposits a like amount of charge on the wire. Proportional counters are rugged, simple devices that have large, x-ray entrance openings and do not require cryogenic refrigeration. Unfortunately, they also have poorer energy resolution. Their inability to separate elements that are close in x-ray energy such as copper and nickel is of little consequence in most industrial and military applications, in which the elemental composition of the aerosolized particles is likely well-known.

The particular proportional counter used in these tests was a Reuter-Stokes type RS-P3-1605-261, a 5-cm-diameter, 15-cm-long cylinder filled with 1 atm of a mixture of 97 percent Xenon and 3 percent Carbon Dioxide. The central wire is 0.0025 cm in diameter and was biased at about 2,000 Volts. To prevent interference by any extraneous primary radiation, the entire cylinder is surrounded by a 0.62-cm-thick, lead-iron-aluminum-graded shield except at the window. Shield considerations are especially important because the detector lies immediately adjacent to the x-ray tube window, separated only by interposed material and a few centimeters.

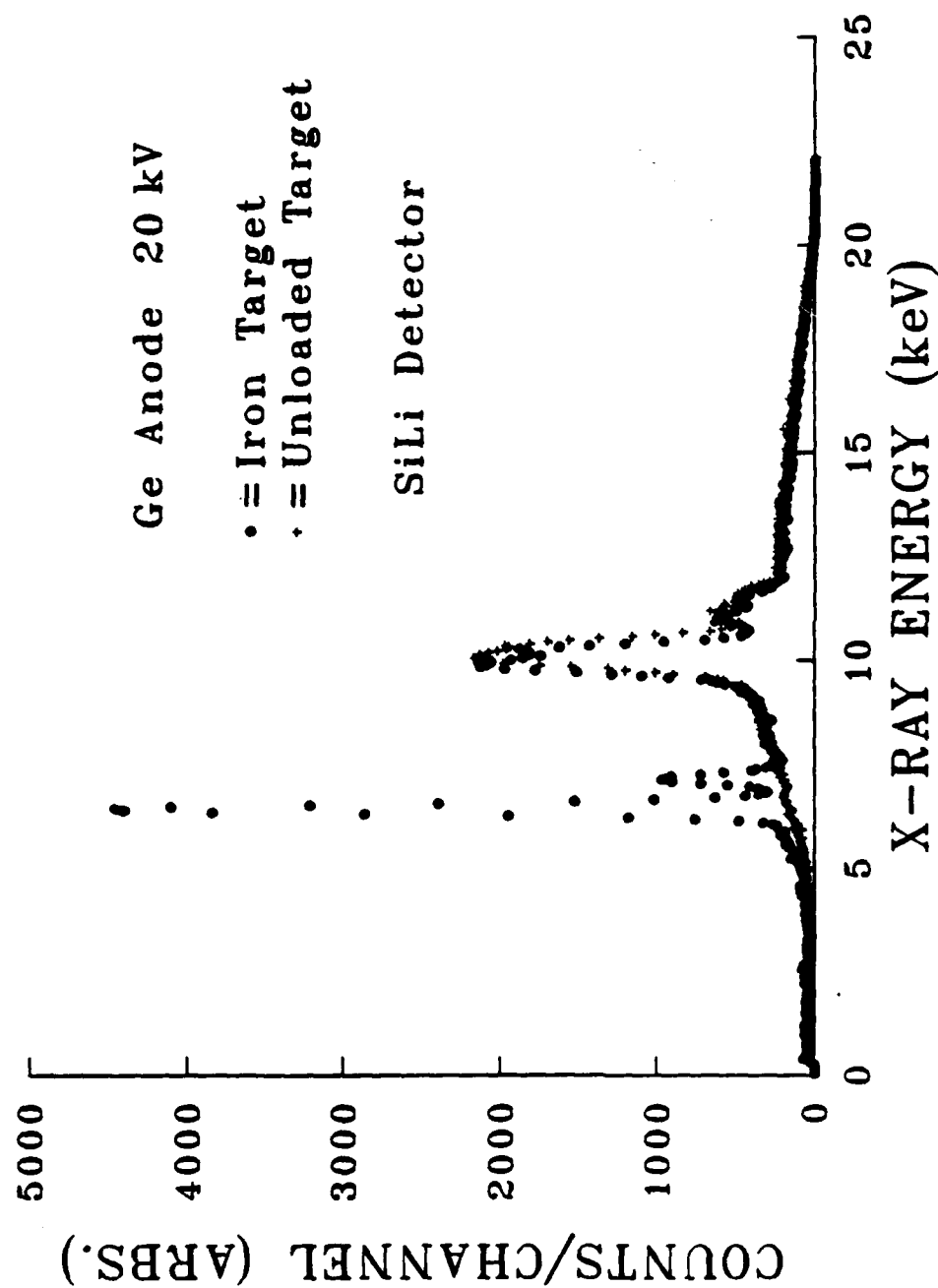


Figure 9. The x-ray spectra output by a SiLi detector when Fe-loaded (upper) and blank (lower) targets are fluoresced with germanium x-rays.

A fluorescence spectrum obtained with a proportional counter is shown in Figure 10. A corresponding spectrum acquired with a SiLi detector appears in Figure 11. The upper curve were acquired with the Fe-loaded target in place, while the lower used a plain paper unloaded target. The inherent resolution advantage of SiLi is obvious. However, note that for the same number of primary x-rays delivered to the target, over 16 times more fluorescent x-rays were detected, a substantial improvement.

3.5. The analysis system. Both the lithium-drifted, silicon detector and the proportional counter have one thing in common -- whenever they are struck by an x-ray photon, they produce an electrical pulse with an amplitude proportional to the x-ray's energy. To convert these pulses into spectra an electronic system depicted in Figure 12 was employed. Besides the detector and its high-voltage, biasing power supply discussed earlier, the system consists of a preamplifier, an amplifier, a baseline restorer, and a multichannel analyzer. Functionally, the preamplifier collects the charge pulse, converts it into a proportionate voltage pulse, and drives that voltage pulse through a long coaxial cable. At the opposite end of the cable, a safe distance from the x-ray tube, the amplifier reshapes the pulse for minimum noise and loss of linearity upon amplification and then amplifies it. Its output is next reshaped by a baseline restorer to correct for undershoot, a source of x-ray energy measurement error at high count rates. The pulse shape at each stage in processing is shown at the top of Figure 12.

Upon leaving the restorer the pulse enters the multichannel analyzer (MCA). This device sorts each pulse according to its amplitude and deposits a count in a category (channel) whose index number is linearly proportional to the amplitude (x-ray energy). As a multitude of pulses are analyzed, the distribution of counts among the channels follows the energy spectra of the incident x-rays. The particular analyzer used, a Nucleus Inc. Quantum 8, can acquire up to four spectra in its memory, each using 256 separate channels. The analyzer outputs pairwise array of channel numbers and corresponding numbers of counts spanning the entire energy spectrum of x-rays accumulated during the time period in which irradiation took place. When the analyzer's internal storage capabilities are filled, the data can be displayed on the internal screen and sent via an internal RS-232C interface to a minicomputer (Tektronix 4052A) and then to a large main frame computer (Digital Equipment Corp. VAX 8600).

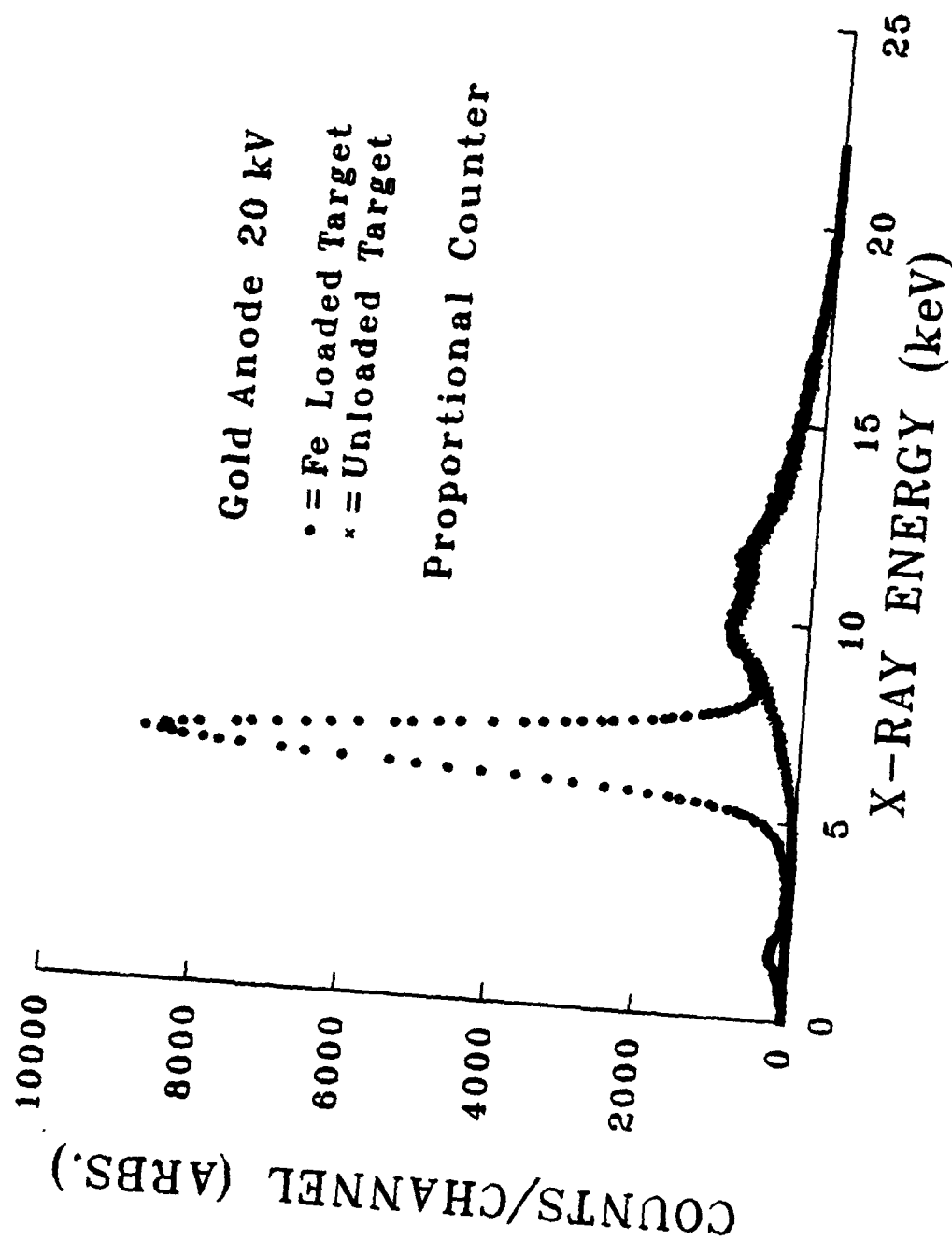


Figure 10. The x-ray spectra output by a proportional counter when Fe-loaded (upper) and blank (lower) targets are fluoresced with gold x-rays.

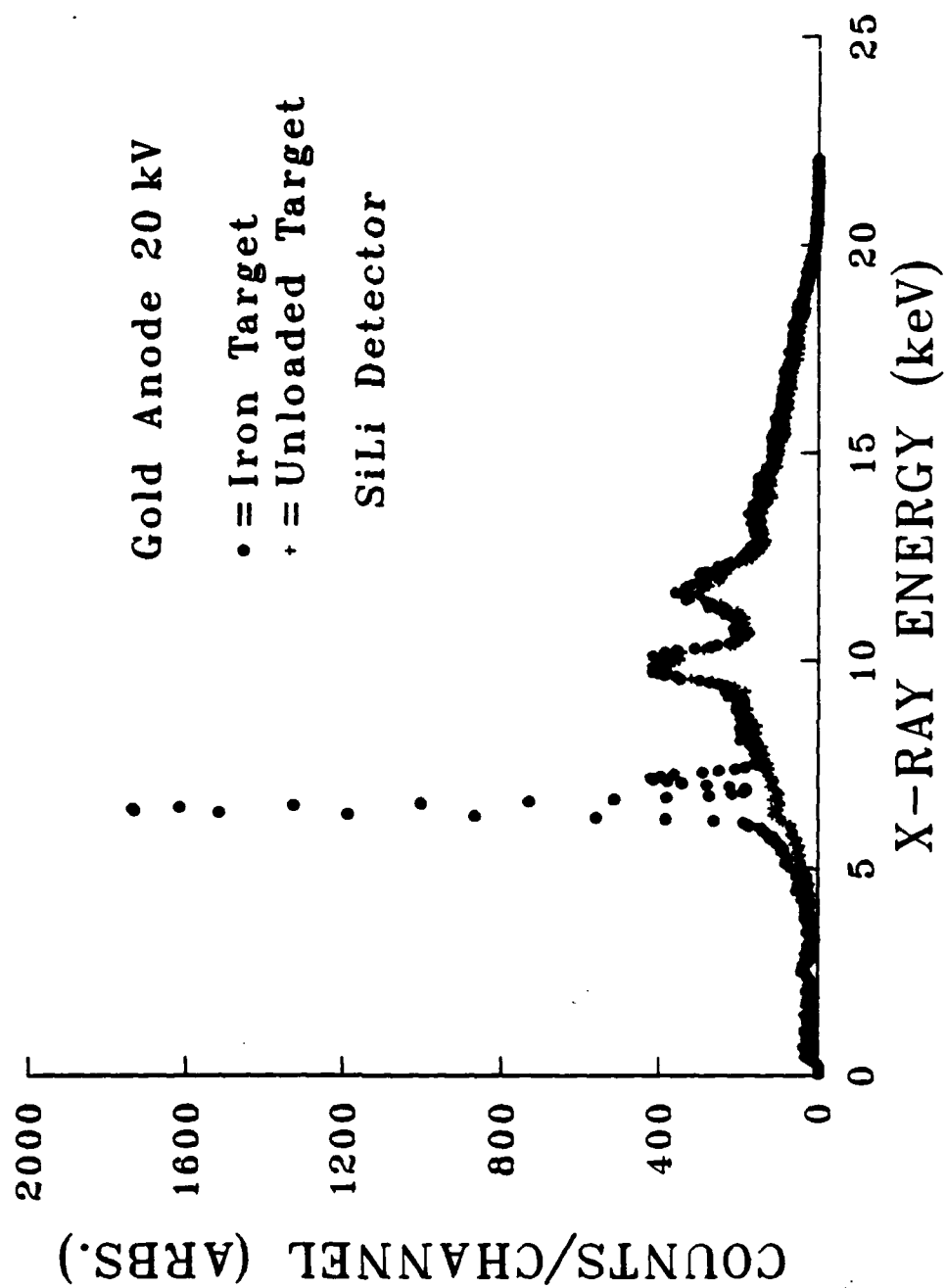


Figure 11. The x-ray spectra output by a SiLi detector when Fe-loaded (upper) and blank (lower) targets are fluoresced with gold x-rays.

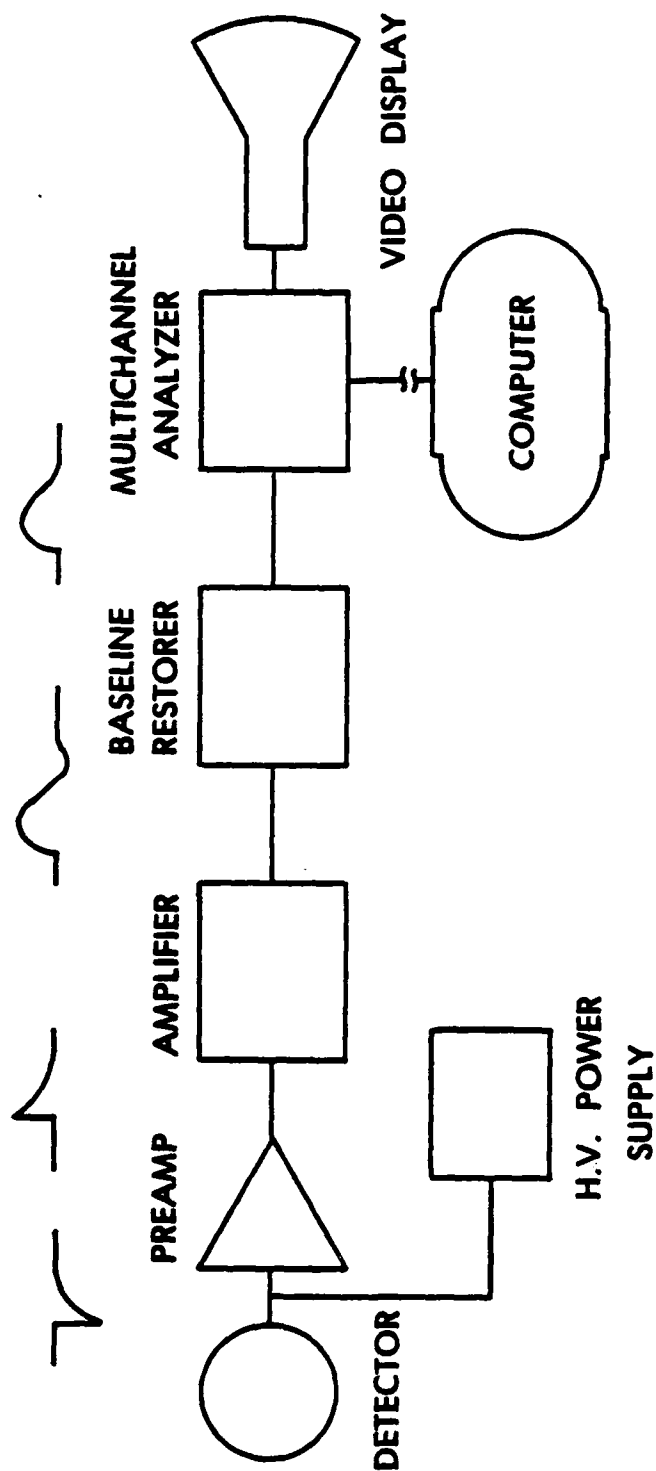


Figure 12. A block diagram of the detection-analysis electronics. The output-pulse shape is depicted above each active component.



Once in the computer, the raw data may be processed and compared with the results of other runs and with the design predictions. This usually has two aspects. First, the MCA channels must be calibrated in energy. This is done by correlating the channel numbers containing the centroids of several elements' characteristic x-ray peaks with tabulated values of their respective energies. The resulting relation for a particular set of detector voltages and amplifier gains is quite linear. By simple interpolation it may be used to identify the energy corresponding to any channel. Once energy calibration is accomplished, the computer is used to rescale and renormalize the raw counts data as required. Usually, this takes the form of either rescaling to a fixed x-ray dose upon the target or renormalizing to a fixed number of detected characteristic x-rays. In either event the raw or processed data is finally displayed upon a video display or other input-output device.

#### 4. THE EXPERIMENT

The essential determination of DXRF's feasibility consists of the irradiation of a suspended target with a given number of primary x-ray photons (dose) from the x-ray tube and a measurement of the number of resulting fluorescence counts. Over the entire operating range of this experiment, the x-ray flux, target density, and raw data count rates were chosen such that the response of the apparatus was linear. This behavior was confirmed in a series of tests and showed that the number of fluorescence counts,  $F$ , observed behaved according to:

$$F = kMit \quad (12)$$

where  $M$  is the mass of material on the target;  $i$  is the anode current in the tube;  $t$  is the exposure time, and  $k$  is a complex function that incorporates the tube-target-detector geometry; the tube voltage and anode material; the overall fluorescence physics; the elemental identity of the target; and the response properties of the detector. As long as the dependence on mass is linear, one can, by simple extrapolation, infer the system's response at higher or lower simulated mass concentrations and x-ray doses. That condition exists until the deposit mass is so high that the count rate capabilities of the data acquisition system are exceeded.

In any actual measurement x-ray counts will come both from fluorescence and from extraneous sources (i.e. backscattered bremsstrahlung.) The origins and size of the extraneous contribution were examined by accumulating three spectra. The first came from the air alone with no suspended

target; the second from air with a blank paper target; and the third from air and a loaded paper target. The first two spectra and the region outside the characteristic region in the third are virtually identical. On the basis of this evidence one may infer that the bremsstrahlung output from the tube backscatters principally from air molecules. Bremsstrahlung's contribution to the spectral region of interest for a given time and primary x-ray flux will be constant over a range of particle concentrations and may be removed by simply subtracting a constant quantity,  $N$ . Like  $F$ ,  $N$  is simply related to the tube current and counting time by:

$$N = nit \quad (13)$$

where  $n$ , like  $k$ , is a complex function of the physical and geometrical makeup of the apparatus as well as its operating parameters.

Before proceeding with a determination of  $k$  we must first consider another question. Any prospective user of this system is probably interested, not only in the response to a specific mass concentration, but is likely to be even more concerned with the smallest mass concentration,  $m$ , which can be measured. The user is further constrained if he wants to carry out the measurement in a fixed time,  $t$ , and is willing to accept a fractional standard deviation in the measurement of target mass of  $s$ . The linear relation between  $F$ ,  $M$ ,  $i$ , and  $t$ , and the high accuracy with which the product of  $i$  and  $t$  can be determined insure that the fractional standard deviation in a measurement of  $M$ ,  $\Delta M/M$ , will be equal to that in the recorded counts  $\Delta F/F$ . The latter uncertainty is dominated by statistical errors. As a starting point note that any determination of the number of the fluorescence counts  $F$  associated with a sample requires two separate measurements of the counts in the fluorescence region -- one from the loaded paper target yielding  $F + N$  counts and one from its unloaded counterpart yielding  $N$ . The value of  $s$  coming from the combination is:

$$\frac{\Delta F}{F} = s = \frac{(F + 2N)^{1/2}}{F} \quad (14)$$

Equation 14 may be solved quadratically for  $F$ . If equation 12 is then substituted, a solution for the mass,  $M$ , is derived. Realizing that, for the unique situation here,  $M$  is numerically equal to the mass concentration of the aerosol simulated; we obtain:

$$M = \frac{1 + (1 + 8Ns^2)^{1/2}}{2s^2 kit} = \frac{1 + (1 + 8nits^2)^{1/2}}{2s^2 kit} = m \quad (15)$$

The value of mass concentration,  $m$ , above is the minimum measurable with a desired fractional standard deviation,  $s$ , in time,  $t$ , given the presence of a spurious count rate,  $N/t$ . All the quantities needed for its computation are readily measured for a specific system and target element.

To determine  $k$ ,  $n$ , and  $M$ , we applied the x-ray flux emanating from the tube while operating at fixed values of  $i$ ,  $V$ , and  $t$  to a suspended target which was designed by the methods of Section 3.3 to simulate a  $1 \text{ gm/m}^3$  aerosol. Next we counted the number of x-rays in the fluorescence region  $F + N$ . The criterion for a pulse being included in  $F$  was that it occupy a portion of the spectrum under the fluorescence peak that lies in the region between those channels having one-half the maximum number of counts. The experiment was repeated, this time using an unloaded paper target suspended at the same distance. The background,  $N$ , was then evaluated and subtracted from the first. The result is  $F$ , a net count corresponding to the expected rate from a  $1 \text{ gm/m}^3$  aerosol.  $F$  may be used as a calibration benchmark (Equation 12), which is valid throughout the linear operating range of the experiment. Knowing  $i$ ,  $t$ ,  $N$  and selecting values for  $s$ , it is then straightforward to arrive at corresponding values for  $k$  via Equation 12; for  $n$  via Equation 13, and for  $m$  via Equation 15.

We must now look at the various factors controlling the performance of this device. Ordinarily, one would like to detect low concentrations in the minimum possible accumulation time. As seen in Equation 15 the value of  $m$  is critically dependent upon the values of  $k$  and  $n$  -- both of which connect the apparatus' performance to its physical composition and geometry. To optimize the apparatus it is thus necessary to undertake a systematic study of  $k$  and  $m$  for various combinations of anode, filter, and detector.

As a starting point one must realize that the basic process underlying this device, photoionization, is at its most effective when the energy of the primary x-ray is equal to that needed to raise an electron bound in the inner shell of a target atom to the lowest continuum states,

the so-called absorption edge. Unfortunately, this energy is so close to that of the fluorescent x-ray that the simple detectors we employ will be unable to unambiguously resolve them. A compromise between photoionization effectiveness and resolution is needed. We did this by recording energy spectra with varying anode material, x-ray tube potential, and filtration both with a blank paper and iron-laden target. Subsequent analysis of the data provided values of  $k$ ,  $n$ , and  $m$  that guided the selection of the optimum conditions. Among the anode materials used were copper (K x-rays at 8.04 keV and 8.90 keV); germanium (K x-rays at 9.89 keV and 10.98 keV); gold (L x-rays at 9.71 keV, 11.43 keV, and 13.37 keV); zirconium (K x-rays at 15.77 keV and 17.66 keV); molybdenum (K x-rays at 17.47 keV and 19.60 Kev), and silver (K x-rays at 22.16 keV and 24.94 keV). For these trials x-ray tube potentials ranged from approximately 15 kV to more than 40 kV in some cases. Appropriate filters, those with good transmission of primary x-rays and poor transmission for bremsstrahlung at fluorescent x-ray energies, were added and several replications were taken.

## 5. RESULTS

5.1 Iron targets. Early in the preliminary tests with this apparatus, it was apparent that, germanium, gold, and, perhaps, copper were the best choices of anode materials for detecting iron targets. Other materials, especially those of greater  $Z$ , required higher tube powers for equivalent fluorescence. Table 1 shows a summary of some of the more important germanium and gold results for cases in which the tube operating potential was 20 kV. The raw data and results shown have been scaled to a common x-ray tube output -- a current of 1 mA and an exposure time of 100 sec. The results have been corrected for the differing fields of view of the two detector types and for an assumed fractional standard deviation of 10 percent. The table includes examples of the system's performance when furnished with a 0.0025-cm-zirconium filter placed over the x-ray tube exit. The thickness value was selected because thicker foils were found to absorb too many primary x-rays for efficient operation, while thinner versions produced a lower backscattered bremsstrahlung suppression.

An examination of Table 1 reveals that, for a fixed tube x-ray output, the optimum performance, that is the lowest value of  $m$ , depends upon the rapid accumulation of counting statistics. Consider the Ge and Au anode results. In both cases using the proportional counter, the addition of a filter with its increased bremsstrahlung rejection barely compensated for the loss of statistical certainty caused by the filters' transmission losses. A glance at the high intrinsic energy resolution SiLi data shows that the filter produces no gain in performance; indeed, it actually results in some degradation.

TABLE 1. One-mA Anode Current Performance, 100 sec.

Detector	Anode	Filter	F counts	N counts	k ( $\times 10^6$ ) counts/A-sec	m mg/m <sup>3</sup>
Prop. Counter	Germanium	none	497956	11148	4.86	3.7
	Germanium	0.0025cm Zirconium	152054	1244	1.51	3.6
	Gold	none	302516	9550	2.93	4.9
	Gold	0.0025cm Zirconium	88550	888	0.876	5.4
	Copper	none	93969	4430	0.895	11.0
SiLi Detector	Germanium	none	21096	50	0.214	7.6
	Germanium	0.0025cm Zirconium	6210	9	0.062	18.6
	Gold	none	18313	376	0.179	18.3
	Gold	0.0025cm Zirconium	5065	16	0.050	24.8
	Copper	none	4856	55	0.048	14.0

The question then arises: Is this the best that can be done? If one can relax the constraints on analysis time,  $t$ , or tolerate higher radiation levels at the analysis site (increased  $i$ ), then the answer is no. Equation 15 shows that  $m$  decreases with increasing  $i$  and  $t$ . Consequently,  $t$  may be increased to whatever the practical limits imposed by measurement goals prescribe with a corresponding decrease in  $m$ . Increases in  $i$  are limited by three factors -- specifically, the environmental x-ray dose one can accept; the count rate limitations of the detector and electronics, and the ability of the x-ray tube to produce increased output. The first limitation is totally dependent upon the application at hand. The second is more directly quantifiable. The highest count rate attainable with a proportional counter is approximately 5,000 counts/sec; while for SiLi's, the limit is 15,000 counts/sec or more. Accordingly, the data base has been used to describe cases where each detector type is counting at its full rate capability. The count rate limitation encompasses all types of x-rays, whether fluorescent or extraneous. The results of those calculations, again corrected for viewfield and employing a fractional standard deviation of 10 percent, appear in Table 2. Included in the same table are calculated values if the anode current,  $I$ , needed to achieve those rates cited. Keep in mind that the values of  $m$  shown in Table 2 represent a practical lower bound on  $m$  for this geometry. Clearly, if one operates the system such that the counts associated with  $m$  saturate its count rate capability, then one could not use it to measure any higher mass concentration, a most unsatisfactory condition.

The full-rate results differ markedly from their fixed-dose counterparts. Note that for the unfiltered proportional counter some degradation appears to take place. This is an artifact of the Table 1 results that recognize no rate limitation. The full-rate results show a clear superiority for SiLi detection. Mass concentrations as low as  $1 \text{ mg/m}^3$  appear to be readily measurable (albeit at some cost - anode currents of 100 mA or more). At this point the last of the three factors limiting the usable, permissible current,  $i$ , -- the ability of the tube to produce such x-ray fluxes -- becomes important. It is governed by the ability of anodes to withstand thermal loads. Germanium anodes could not be run at dissipations above 25 W and accelerating potentials of 25 kV without vaporization-induced electrical breakdown of the x-ray tube. Gold, on the other hand, was capable of several hundreds of watts. This advantage, as pointed out already, is likely due to a combination of gold's higher melting point and better thermal conductivity and, ultimately, will be a governing factor in any high count rate operation.

5.2 Copper targets. A series of tests similar to those described above using the same selection of anodes, except a copper target, was carried out. It demonstrated that zirconium anodes offered the best extraneous counts versus fluorescence output compromise, and that zirconium was a good refractory anode material. It was observed that, at equal tube currents and voltages, the primary zirconium x-ray flux was less than the corresponding gold and germanium levels. However, the copper fluorescence output, though smaller, did not exhibit a drop of equal magnitude. This behavior may be attributed to the lower absorption of the primary and fluorescent x-rays by the air and to copper's higher value of the physical fluorescence yield.

TABLE 2. Count Rate Limited Performance, 100 sec.

Detector	Anode	Filter	Loaded Counts	Bkgd Counts	I	m
Prop. Counter	Germanium	none	237647	5320	0.47	4.66
	Germanium	0.0025cm Zirconium	233942	1914	1.53	2.81
	Gold	none	228376	7209	0.75	5.61
	Gold	0.0025cm Zirconium	206541	2071	2.33	3.42
	Copper	none	244894	11545	2.60	6.70
SiLi Detector	Germanium	none	781710	4885	36.8	1.33
	Germanium	0.0025cm Zirconium	847366	1444	138.3	0.69
	Gold	none	499149	7903	29.1	2.61
	Gold	0.0025cm Zirconium	526328	1799	107.5	1.24
	Copper	none	591180	7135	128.2	2.12

5.3 Tests at higher tube voltages. Several exploratory measurements were made using accelerating potentials of 30 kV and 40 kV. Unfortunately, it was not possible to derive complete sets of data at these potentials due to difficulties in manually stabilizing the x-ray tube outputs over long periods of time. Nonetheless, some conclusions can be drawn. A substantial improvement in the ratio of F to N in going from 20 kV to 30 kV was observed, at least a factor of 2 to 3. In going from 30 kV to 40 kV, less improvement was found. The characteristic photon output per watt of anode power also improved considerably with increasing potential. However, operating the tube with nonrefractory anodes (especially Germanium) became very difficult due to frequent sparkover. For most materials sparkover could be alleviated somewhat by conditioning the anode, that is, operating the tube at a few watts and 40 kV for an hour or so before higher powers were attempted. A microscopic examination of a "conditioned" anode showed it to be smoother overall and less granular on its surface than raw anode stock. Presumably, electron bombardment both eroded and annealed its surface.

## 6. CONCLUSION AND SUGGESTIONS

There seems to be little doubt that x-ray fluorescence can provide an effective diagnostic tool in some aerosol tasks. It can work on brass, iron, copper and any other material whose atomic number is 24 or above. DXRF's primary advantages are an ability to operate directly upon the aerosol as dispersed, simplicity, ease of absolute calibration, applicability over a wide concentration range, ruggedness, and speed. Its drawbacks include the use of ionizing radiation in external areas and the potential for mishap with the high voltages associated with x-ray production -- all problems that can be resolved via careful design.

From the lessons learned in these tests, one may draw some conclusions about improving DXRF system design. A schematic drawing of one suggested version is shown in Figure 13. Although its major features are quite similar to those of the present prototype, there are important differences in detail. The most significant change is in the detector. From the computational results shown in Figure 8, it is easy to see that efficient detection of fluorescence, originating relatively close to the x-ray tube, is very important. Assuming that a second-generation DXRF device will utilize a standard commercial-end or side-window x-ray tube, one can achieve an



improved detection geometry by adopting an annular detector aligned coaxially with the tubes output. Extensive shielding of the detector from primary direct irradiation by the tube must be incorporated into a design such as this. Furthermore, it is also important to control extraneous backscattering from the near-exit air. For that problem collimation of the primary x-rays can help. Insertion of a coaxial aluminum sleeve of variable length will serve, not only to collimate the x-rays, but also to set the field of view of the detector. Additional collimation may serve yet another useful function. Backscattering is at a minimum for angles near 90 degrees, while fluorescence is approximately isotropic. It would likely be worthwhile to study the benefits of restricting attention to large off-axis angles in hopes of realizing further relative suppression of backscattering.

Regardless of its detailed geometry a next-generation device should be able to take advantage of the recent advances in compact x-ray tube design. Most DRXF on aerosols will likely involve tubes operating at 30 kV - 60 kV. For such situations it is possible to purchase tube, power supply, and detector combinations that would easily fit into a small suitcase and weigh 15 kg or less. The complete analysis system, amplifiers, multichannel analyzers, displays, etc., could also be placed in a similar-sized package. For most applications, one would likely want to separate the system from its mating unit by a distance of several meters. Whatever its configuration, the full potential of any DXRF device, including those proposed here, cannot be fully assessed until tested upon real aerosols in large test chambers or, better still, in the field.

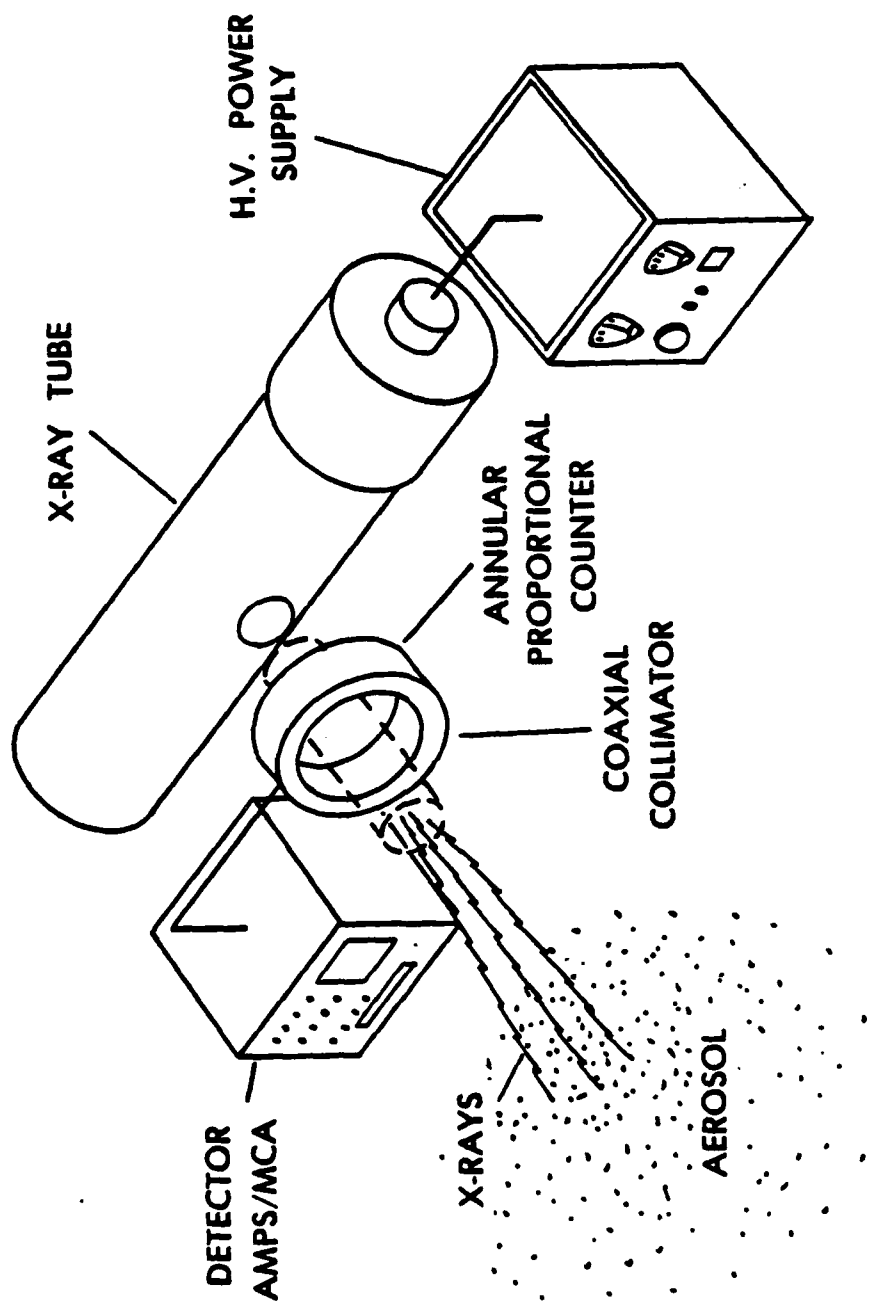


Figure 13. An improved direct-fluorescence device.

## 7. REFERENCES

1. "Air Sampling Instruments for Evaluation of Atmospheric Contaminants," American Conference of Governmental Industrial Hygienists, Cincinnati, Ohio, 5th ed. (1978).
2. Lundgren, D., et.al., "Aerosol Mass Measurement Using Piezoelectric Crystal Sensors," Fine Particles, B.Y. Liu - ed.; Academic Press, New York, NY (1976).
3. Von Brand, E.K., "Applications of a Continuous Portable Smoke Recorder," Mechanical Engineering (ASME) June 1950.
4. Macias, E.S., and Husar, R.B., "Atmospheric Particulate Mass Measurement with Beta Attenuation Mass Monitor," Environmental Science and Technology, 10, 904 (1976).
5. Pungor, E., and Polos, L., "Emission and Atomic Absorption Spectroscopy," Analysis of Airborne Particles by Physical Methods, H. Malissa - ed.; CRC Press, West Palm Beach, Florida, (1978).
6. Coenen, W., "Registrierende Stabmessung nach der Methode der Kleinionen-anlagerung," Staub, 24, S350 (1964).
7. Examples of such devices include: (a) Aerosol Particle Counting System, Bausch and Lomb, Rochester, N.Y.; (b) Stack Transmissometer, Lear Siegler Environmental Tech Division, Englewood, Colorado.
8. Thomson, G., et.al., "Near Real-Time Elemental Mass Concentration Measurements of Medium and High Z Aerosols using X-ray Fluorescence," Review of Scientific Instruments. -- to be published.
9. Coisson, R., "X-ray Sources," Imaging Processes and Coherence in Physics, M. Schlenker - ed., Springer-Verlag, Berlin (1980).
10. Evans, R.D., The Atomic Nucleus, McGraw-Hill, New York, NY (1955).

# DISTRIBUTION LIST

<u>No of Copies</u>	<u>Organization</u>	<u>No of Copies</u>	<u>Organization</u>
12	Administrator Defense Technical Info Center ATTN: DTIC-DDA Cameron Station Alexandria, VA 22304-6145	1	Director US Army Aviation Research and Technology Activity Ames Research Center Moffett Field, CA 94035-1099
1	HQDA (SARD-TR) Washington, DC 20310-0001	1	Commander US Army Missile Command ATTN: AMSMI-RD-CS-R (DOC) Redstone Arsenal, AL 35898-5241
1	Commander US Army Materiel Command ATTN: AMCDRA-ST 5001 Eisenhower Avenue Alexandria, VA 22333-0001	1	Commander US Army Tank Automotive Command ATTN: ASQNC-TAC-DI (Technical Library) Warren, MI 48397-5000
1	Commander US Army Laboratory Command ATTN: AMSLC-DL Adelphi, MD 20783-1145	1	Director US Army TRADOC Analysis Command ATTN: ATAA-SL White Sands Missile Range, NM 88002-5502
2	Commander Armament RD&E Center US Army AMCCOM ATTN: SMCAR-MSI Picatinny Arsenal, NJ 07806-5000	1	Commandant US Army Infantry School ATTN: ATSH-CD-CSO-OR Fort Benning, GA 31905-5660
2	Commander Armament RD&E Center US Army AMCCOM ATTN: SMCAR-TDC Picatinny Arsenal, NJ 07806-5000	1	AFWL/SUL Kirtland AFB, NM 87117-5800
1	Director Benet Weapons Laboratory Armament RD&E Center US Army AMCCOM ATTN: SMCAR-LCB-TL Watervliet, NY 12189-4050	1	Air Force Armament Laboratory ATTN: AFATL/DLODL Eglin AFB, FL 32542-5000
1	Commander US Army Armament, Munitions and Chemical Command ATTN: SMCAR-ESP-L Rock Island, IL 61299-5000		<u>Aberdeen Proving Ground</u> Dir, USAMSAA ATTN: AMXSY-D AMXSY-MP, H. Cohen Cdr, USATECOM ATTN: AMSTE-TO-F Cdr, CRDEC, AMCCOM ATTN: SMCCR-RSP-A SMCCR-MU SMCCR-SPS-IL
1	Commander US Army Aviation Systems Command ATTN: AMSAV-DACL 4300 Goodfellow Blvd. St. Louis, MO 63120-1798		

# DISTRIBUTION LIST

<u>No of Copies</u>	<u>Organization</u>
1	Program Manager-SMOKE ATTN: AMCPM-SMK (Col. Joseph Phillip) Bldg. 324
12	US Army Ballistic Research Laboratory Terminal Ballistics Division ATTN: SLCBR-TB-EP (Dr. Donald Eccleshall) SLCBR-TB-EP (Dr. Andrus Niiler) SLCBR-TB-EP (Dr. John Powell) SLCBR-TB-EP (Charles Stumpf)el) SLCBR-TB-EP (Alex Zielinski) SLCBR-TB-EP (Henry Burden) SLCBR-TB-EP (Dr. Arthur Gauss) SLCBR-TB-EP (Dr. Steve Cornelison) SLCBR-TB-EP (Lazlo Kecskes) SLCBR-TB-EP (Dr. Thomas Kottke) SLCBR-TB-EP (Dr. Robert Bossoli) SLCBR-TB-EP (Dr. Clint Hollandsworth)
	<u>Aberdeen Proving Ground-EA</u>
12	US Army Chemical RD&E Center ATTN: SMCCR-MU (Dir, LTC John Plummer, Munitions Directorate) SMCCR-MUS (Merlin Erickson, Smoke Div.) SMCCR-MUS-S (John Green, Smoke Screening Br.) SMCCR-MUS-T (Horace Pearce, Tactical Obs. Br.) SMCCR-MUS-A (Joseph Wienand, Smoke Tech. Br.) SMCCR-MUT (Drew Farenwald, Tech. Integration Div.) SMCCR-DD (Dr. John Ferriter, Detection Dir.) SMCCR-RS (Dr. Ray Mackay, Research Dir.) SMCCR-RSP (Dr. Art Stuempfle, Physics Div.) SMCCR-RSP-B (Dr. J. Embury, Obscuration Sciences Div.) SMCCR-RST (Dr. Sandra Thomson, Toxicology Div.) SMCCR-SF (Jim Cannon, Safety Office) Aberdeen Proving Ground, MD 21010

USER EVALUATION SHEET/CHANGE OF ADDRESS

This laboratory undertakes a continuing effort to improve the quality of the reports it publishes. Your comments/answers below will aid us in our efforts.

1. Does this report satisfy a need? (Comment on purpose, related project, or other area of interest for which the report will be used.) \_\_\_\_\_  
\_\_\_\_\_
2. How, specifically, is the report being used? (Information source, design data, procedure, source of ideas, etc.) \_\_\_\_\_  
\_\_\_\_\_
3. Has the information in this report led to any quantitative savings as far as man-hours or dollars saved, operating costs avoided, or efficiencies achieved, etc? If so, please elaborate. \_\_\_\_\_  
\_\_\_\_\_
4. General Comments. What do you think should be changed to improve future reports? (Indicate changes to organization, technical content, format, etc.) \_\_\_\_\_  
\_\_\_\_\_

BRL Report Number \_\_\_\_\_ Division Symbol \_\_\_\_\_

Check here if desire to be removed from distribution list. \_\_\_\_\_

Check here for address change. \_\_\_\_\_

Current address: Organization \_\_\_\_\_  
Address \_\_\_\_\_  
\_\_\_\_\_

-----FOLD AND TAPE CLOSED-----

Director  
U.S. Army Ballistic Research Laboratory  
ATTN: SLCBR-DD-T(NEI)  
Aberdeen Proving Ground, MD 21005-5066

OFFICIAL BUSINESS  
PENALTY FOR PRIVATE USE \$300



NO POSTAGE  
NECESSARY  
IF MAILED  
IN THE  
UNITED STATES

Director  
U.S. Army Ballistic Research Laboratory  
ATTN: SLCBR-DD-T(NEI)  
Aberdeen Proving Ground, MD 21005-9989